ISSN: 2161-7570 Volume 5, Number 1, January 2015

Scientific Research Publishing

Open Journal of Geology

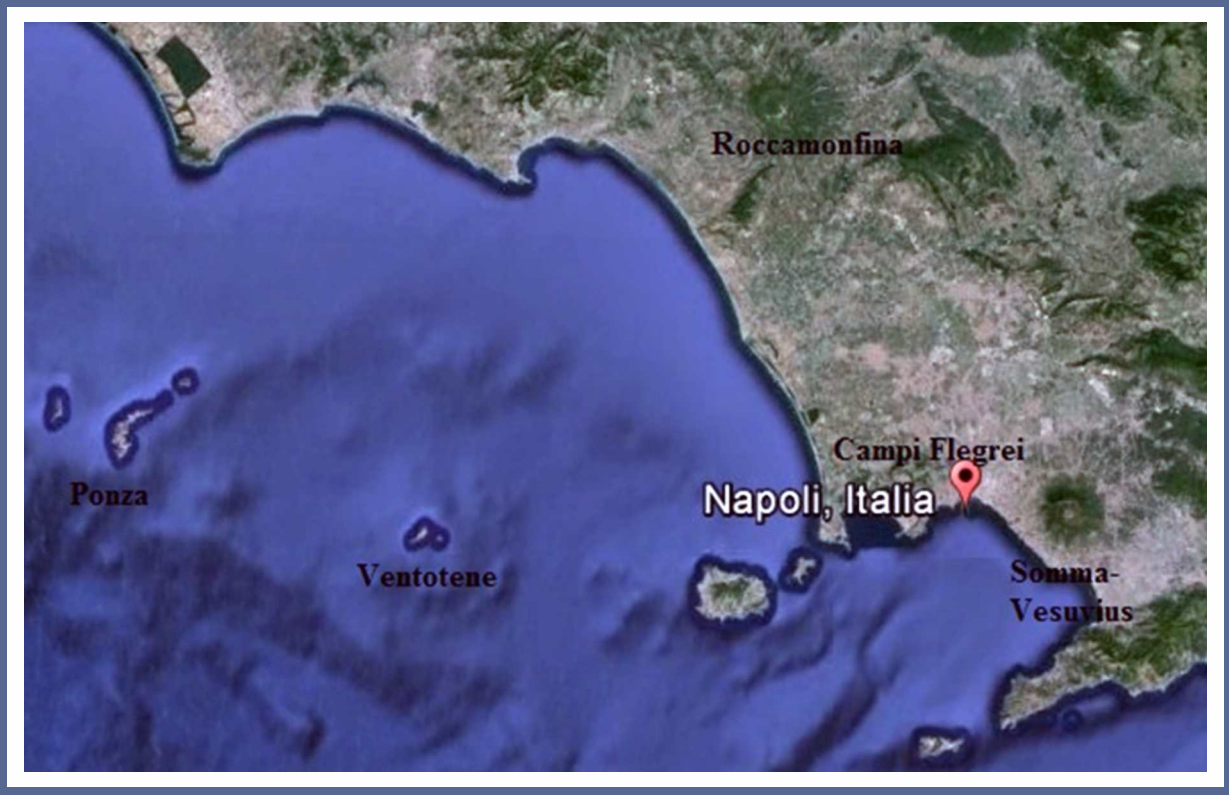

ISSN: 2161-7570

www.scirp.org/journal/ojg

Journal Editorial Board

ISSN 2161-7570 (Print) ISSN 2161-7589 (Online)
http://www.scirp.org/journal/ojg

Editor-in-Chief

Prof. Zhihong Wang Chinese Academy of Sciences, China

Editorial Board

Prof. Md. Mahmudul Alam Kyoto University, Japan
Prof. Mohammad Ayaz Alam Universidad de Chile, Chile
Dr. Ranjith P. Gamage Monash University, Australia
Prof. Girish Gopinath Centre for Water Resources Development and Management, India
Prof. Alexandra Guedes University of Porto, Portugal
Prof. Mohamed Tahir Hussein King Saud University, Saudi Arabia
Prof. Ali Ihsan Karayigit Hacettepe University, Turkey
Prof. Gang Li Chinese Academy of Sciences, China
Dr. Tranos D. Markos Aristotle University of Thessaloniki, Greece
Dr. Mostafa Tantawy Mohamed Assiut University, Egypt
Prof. Gopalakrishnarao Parthasarathy CSIR-National Geophysical Research Institute, India
Prof. Tokiyuki Sato Akita University, Japan
Prof. Ian P. Skilling University of Pittsburgh, USA
Prof. Alireza K. Somarin Brandon University, Canada
Prof. Juan R. Tejerina University of Cantabria, Spain
Dr. Ergün Tuncay Hacettepe University, Turkey
Prof. Shunshan Xu National University of Mexico, Mexico
Prof. Xiaoli Yang Central South University, China
Prof. Hong Zheng Chinese Academy of Sciences, China

Open Journal of Geology, 2015, 5, 1-37
Published Online January 2015 in SciRes. http://www.scirp.org/journal/ojg

Table of Contents

Volume 5 Number 1 January 2015

The figure on the front cover is from the article published in Open Journal of Geology, 2015, Vol. 5, No. 1, pp. 1-12 by Angelo Paone.

Open Journal of Geology (OJG)

Journal Information

SUBSCRIPTIONS

The *Open Journal of Geology* (Online at Scientific Research Publishing, www.SciRP.org) is published monthly by Scientific Research Publishing, Inc., USA.

Subscription rates:

Print: $79 per issue.
To subscribe, please contact Journals Subscriptions Department, E-mail: sub@scirp.org

SERVICES

Advertisements
Advertisement Sales Department, E-mail: service@scirp.org

Reprints (minimum quantity 100 copies)
Reprints Co-ordinator, Scientific Research Publishing, Inc., USA.
E-mail: sub@scirp.org

COPYRIGHT

COPYRIGHT AND REUSE RIGHTS FOR THE FRONT MATTER OF THE JOURNAL:

Copyright © 2015 by Scientific Research Publishing Inc.

This work is licensed under the Creative Commons Attribution International License (CC BY).
http://creativecommons.org/licenses/by/4.0/

COPYRIGHT FOR INDIVIDUAL PAPERS OF THE JOURNAL:

Copyright © 2015 by author(s) and Scientific Research Publishing Inc.

REUSE RIGHTS FOR INDIVIDUAL PAPERS:

Note: At SCIRP authors can choose between CC BY and CC BY-NC. Please consult each paper for its reuse rights.

DISCLAIMER OF LIABILITY

Statements and opinions expressed in the articles and communications are those of the individual contributors and not the statements and opinion of Scientific Research Publishing, Inc. We assume no responsibility or liability for any damage or injury to persons or property arising out of the use of any materials, instructions, methods or ideas contained herein. We expressly disclaim any implied warranties of merchantability or fitness for a particular purpose. If expert assistance is required, the services of a competent professional person should be sought.

PRODUCTION INFORMATION

For manuscripts that have been accepted for publication, please contact:
E-mail: ojg@scirp.org

Open Journal of Geology, 2015, 5, 1-12
Published Online January 2015 in SciRes. http://www.scirp.org/journal/ojg
http://dx.doi.org/10.4236/ojg.2015.51001

Pb Isotopes Data from the Campanian Volcanic Province: A Model to Generate These Distinctive Pb Isotopic Variations

Angelo Paone[1,2]

[1]United States Geological Survay, Reston, USA
[2]Dipartimento di Scienze della Terra, Università degli Studi di Napoli "Federico II", Naples, Italy
Email: angelo.paone1@gmail.com

Received 20 December 2014; accepted 11 January 2015; published 20 January 2015

Copyright © 2015 by author and Scientific Research Publishing Inc.
This work is licensed under the Creative Commons Attribution International License (CC BY).
http://creativecommons.org/licenses/by/4.0/
Open Access

Abstract

A broad set of samples from the CVP has been analyzing Pb isotopes. Campanian Volcanic Province (CVP) has been produced by various ranges of mixing between three components: 1) MORB, 2) Hercynian basement and 3) upper crust. Anyhow, the upper crust that has modified the Pb isotopic composition also shows trends towards an Achaean upper crust. This is consistent for all Mediterranean area. This is not in contrast with the past plate tectonic reconstruction. Also the surface sediments (GLOSS) may have been a mixing between the Achaean upper crust and a Hercynian component with an implication worldwide due to the rock cycle processes.

Keywords

Pb Isotopes, Campanian Volcanic Province, Hercynian, Sediments, MORB

1. Introduction

The Campanian Volcanic Province (**Figure 1**) is made of the following volcanic area: Somma-Vesuvius volcano [1], Campi Flegrei Volcanic District [2] [3], Roccamonfina volcano [3] and the Island of Ponza and Ventotene [4]. A tectonic scenario has been envisaged on the basis of geophysical, petrologic and geochemical data, where the magma is stored in the deep and hot intrusion zone [4]-[6]. The magmas erupted have a sediments signature due to the adjacent Adria slab subducting [4] [7]. Tomographic results confirm this scenario ([8], references therein). In this report, I would like to unravel the features of the Pb isotopes data from the Campanian Volcanic Province [9]-[11]. Moreover, a model is built to explain these typical Pb isotopes signatures.

How to cite this paper: Paone, A. (2015) Pb Isotopes Data from the Campanian Volcanic Province: A Model to Generate These Distinctive Pb Isotopic Variations. *Open Journal of Geology*, **5**, 1-12. http://dx.doi.org/10.4236/ojg.2015.51001

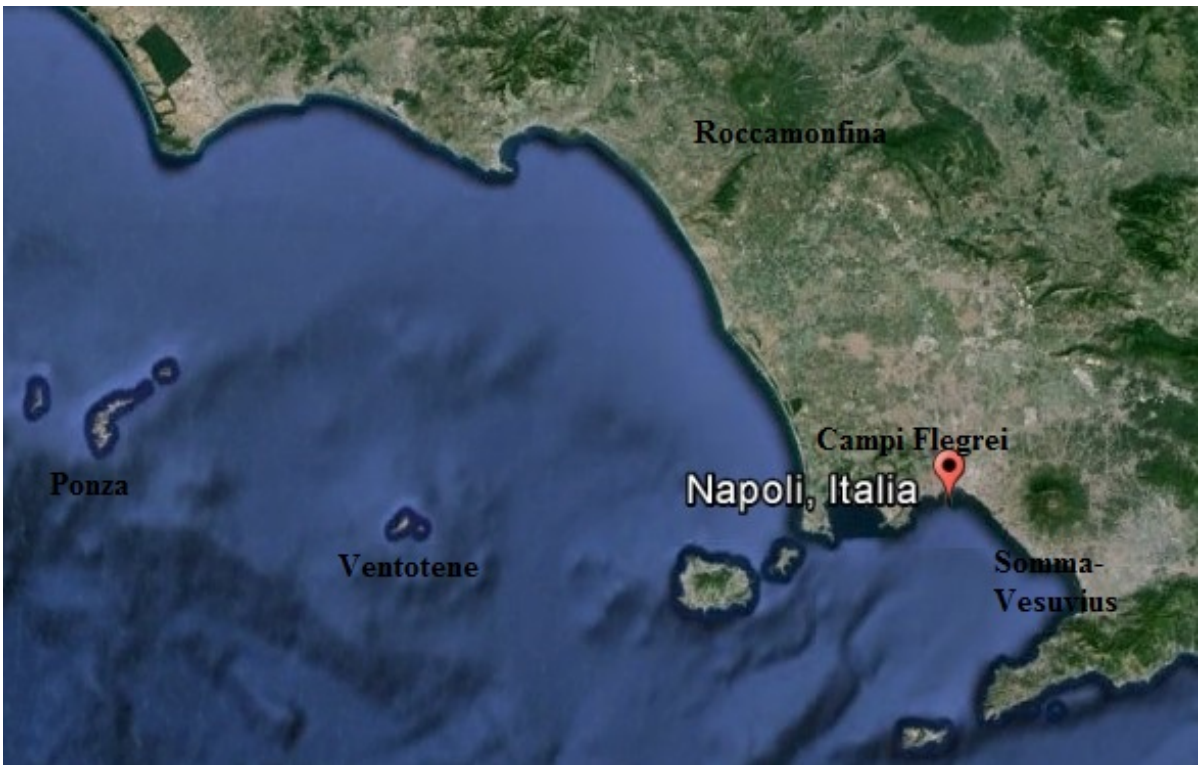

Figure 1. Aerial photograph of the main volcanic area of the Campanian Volcanic Province.

2. A Geochemical Overview to Summarize the Magmatic Origin and Crustal Effects in Campanian Volcanic Province

The Campanian Volcanic Province is part of the classic western potassic volcanic province of the Italian Peninsula. The Campanian volcanic products show the effects of shallow assimilation and fractional crystallization, and the contribution of regional crustal sources (e.g., Hercynian basement-Calabrian crust). The Roccamonfina, Campi Flegrei, and Ventotene volcanic rocks are characterised by wide isotopic and geochemical variations. Such variations appear to reflect both AFC processes and chemical heterogeneity in the upper mantle that may be linked to subduction processes. Mixing curves (Th/Ce-, Ba/K- and Eu/Eu*-$^{143}Nd/^{144}Nd$) linking sediments and mantle end-members account for the variations in the Campanian Province volcanic rocks with a sediment contribution of 2% - 10%. The upper mantle sources for the low- and high-K rocks at Roccamonfina have been constrained on the basis of a multi-element normalized diagram. The two sources require different amounts of sediment in the mantle wedge (LK~2% versus HK~10%) and a fluid component probably from altered ocean crust to explain the fluid mobile elements. Low-K Roccamonfina rocks are geochemically similar to those from Campi Flegrei, Ventotene, and Somma-Vesuvius, suggesting a similar proportion of sediment in their upper mantle source regions [3].

3. Sampling and Analytical Techniques

A representative suite of 300 volcanic rocks of samples was obtained on and around the flanks of Mount Somma-Vesuvius volcano, Roccamonfina volcano, Campi Flegrei Volcanic District and Ventotene Island on the basis of detailed field mapping (Rolandi, unpubl. Data); each rocks weighted 2 Kg, then was crushed to ash size, 2 g for each rocks were analyzed for Pb isotopic determinations. At least half of the samples are pumice and the rest are scoria and lava. Pb isotopes were determined at the US Geological Survey, Reston, VA, on a Finnigan-MAT 262 mass spectrometer. Pb isotopic analyses were done on 50 minerals separates (plagioclase, sanidine, and leucite). And 250 whole rocks (total of ~300 samples, **Table 1** and **Table 2**), using static multi-collection mode. Isotopes were separated using standard anion-exchange methods: Pb isotopic ratios were normalized for mass fractionation by 0.1% per mass unit on the basis of repeated runs of NBS-981; Pb blanks during

Table 1. Pb isotopic composition of the volcanic rocks and minerals from Mt. Somma-Vesuvius volcano.

Sample ID		$^{206}Pb/^{204}Pb$	SE(M)2	$^{207}Pb/^{204}Pb$	SE(M)2	$^{208}Pb/^{204}Pb$	SE(M)2
S1a	WR	19.002	0.001	15.625	0.008	38.985	0.002
S1a	WR	19.053	0.003	15.681	0.003	39.169	0.009
S1a	KSP	19.127	0.042	15.752	0.036	39.349	0.092
S1b	WR	19.013	0.003	15.633	0.003	39.014	0.007
S1b	WR	19.041	0.002	15.664	0.001	39.121	0.005
S1b	KSP	19.038	0.007	15.664	0.007	39.124	0.019
S1c	WR	19.023	0.001	15.642	0.001	39.037	0.003
S1c	KSP	19.039	0.002	15.661	0.002	39.105	0.006
S1d	WR	19.002	0.0006	15.610	0.0005	38.935	0.001
S1d	WR	18.994	0.002	15.607	0.001	38.925	0.003
S2(1)	WR	19.030	0.005	15.621	0.005	39.032	0.035
S2(1)	WR	19.033	0.003	15.629	0.003	38.986	0.007
S2(1)	KSP	19.016	0.082	15.640	0.066	39.087	0.166
S2(2)a	WR	19.042	0.006	15.637	0.005	39.013	0.014
S2(2)a	KSP	19.538	0.678	16.040	0.552	39.915	1.459
S2(2)b	WR	18.990	0.006	15.689	0.006	39.149	0.017
S2(2)b	WR	18.931	0.002	15.611	0.001	38.893	0.003
S2(2)c	KSP	18.982		15.682		39.135	
S2(2)e	WR	18.985		15.639		38.987	
S2(3)	KSP	18.979	0.003	15.666	0.003	39.085	0.007
S2(4)	WR	18.958		15.645		39.024	0.003
S3(1)a	KSP	18.949	0.001	15.626	0.001	38.950	
S3(1)b	WR	18.966		15.658		39.067	0.004
S3(1)b	KSP	18.950	0.001	15.629	0.001	38.955	
S3(1)c	WR	18.949		15.637		38.995	0.004
S3(1)c	KSP	18.954	0.001	15.635	0.001	38.978	
S3(1)d	WR	19.004		15.702		39.223	0.009
S3(1)d	KSP	18.947	0.004	15.627	0.003	38.952	
S3(1)e	WR	18.935		15.623		38.946	0.004
S3(1)e	KSP	18.968	0.002	15.652	0.001	39.043	0.006
S3(1)f	WR	18.916	0.002	15.592	0.002	38.830	
S3(2)a	WR	18.960		15.647		39.031	0.004
S3(2)b	WR	18.941	0.002	15.615	0.001	38.914	0.002
S3(2)c	WR	18.937	0.0007	15.613	0.0006	38.904	0.009
S3(2)c	WR	18.909	0.005	15.597	0.003	38.851	0.004
S3(2)d	WR	18.944	0.002	15.622	0.001	38.936	0.001
S3(2)e	WR	18.936	0.0006	15.612	0.0005	38.901	0.007
S3(2)e	WR	18.949	0.002	15.629	0.002	38.956	

Continued

S3(2)f	WR	18.959		15.645		39.025	0.002
S3(3)a	WR	18.940	0.001	15.614	0.001	38.908	
S3(3)a	WR	18.975		15.667		39.098	0.004
S3(3)b	WR	18.956	0.001	15.636	0.001	38.981	
S3(3)b	WR	18.947		15.646		39.015	
S3(3)c	KSP	18.956	0.001	15.638	0.001	38.984	0.004
S3(3)c	KSP	18.975		15.669		39.101	
S3(3)c	WR	18.931	0.0008	15.613	0.0008	38.902	0.002
S3(3)d	WR	18.945	0.0006	15.624	0.0006	38.938	0.002
S4(2)a	WR	18.936	0.0006	15.604	0.0006	38.874	0.001
S4(2)a	WR	18.959	0.004	15.636	0.004	38.980	0.011
S4(2)b	WR	18.963		15.656		39.051	
S4(2)b	WR	18.936	0.0009	15.604	0.0008	38.874	0.002
S4(4)#1	WR	18.944	0.002	15.624	0.002	38.934	0.007
S5(1)b	WR	19.053		15.769		39.430	
S5(1)c	WR	19.034	0.006	15.737	0.006	39.312	0.018
S5(2)a	WR	18.953	0.0007	15.629	0.0007	38.949	0.002
S5(2)a	WR	18.960	0.004	15.647	0.004	39.015	0.014
S5(2)a	KSP	19.001	0.005	15.684	0.005	39.140	0.016
S5(2)a	KSP	19.020		15.715		39.257	
S5(2)b	WR	18.967	0.001	15.648	0.001	39.011	0.004
S5(2)b	KSP	18.979	0.002	15.657	0.002	39.050	0.007
S5(3)a	WR	19.030		15.736		39.320	
S5(3)b	WR	19.011	0.005	15.705	0.004	39.202	0.012
S5(4)b	WR	18.953	0.002	15.609	0.002	38.887	0.005
S5(4)b	WR	18.953	0.0009	15.615	0.0008	38.899	0.002
S6(1)a	WR	18.953	0.0009	15.622	0.0008	38.927	
S6(1)a	KSP	18.950	0.001	15.623	0.002	38.933	0.002
S6(1)b	WR	18.933	0.001	15.603	0.001	38.863	0.006
S6(1)b	KSP	18.944	0.002	15.618	0.002	38.912	0.003
S6(1)c	WR	18.939	0.0008	15.611	0.0007	38.890	0.005
S6(1)c	KSP	18.983	0.003	15.663	0.003	39.069	0.002
S6(2)a	WR	18.971	0.002	15.662	0.002	39.051	0.008
S6(2)a	WR	18.962	0.0008	15.640	0.0008	38.986	0.005
S6(2)a	KSP	19.003	0.009	15.686	0.009	39.140	0.002
S9(1)a	KSP	19.384	0.139	16.041	0.114	40.168	0.027
S9(1)a	KSP	18.995		15.688		39.148	0.298
S9(1)b	KSP	18.978		15.664		39.084	
S9(1)b	Sink	18.959	0.001	15.633	0.001	38.967	

Continued

S9(1)c	KSP	18.987		15.683		39.146	0.003
S9(1)d	WR	18.947	0.001	15.618	0.0009	38.916	
S10(1)a	KSP	18.963	0.002	15.634	0.002	38.960	0.002
S10(1)a	KSP	18.982		15.666		39.076	0.005
S10(1)c	KSP	19.010		15.687		39.161	
S10(1)d	WR	18.959	0.001	15.608	0.001	38.887	
S11(1)	WR	18.948	0.0007	15.622	0.0006	38.913	0.003
S12(2)	WR	18.982		15.695		39.174	0.0016
S13(1)a	WR	18.963	0.008	15.664	0.007	39.057	
S13(1)a	WR	18.963		15.664		39.057	0.017
S13(1)b	WR	18.940	0.001	15.609	0.001	38.881	
S13(2)b	WR	18.974		15.673		39.099	0.003
S14(1)	WR	18.955	0.002	15.641	0.002	38.982	
S14(2)	WR	18.968		15.654		39.032	0.006
S15(1)b	WR	18.949	0.003	15.623	0.003	38.915	
S15(1)b	WR	19.017		15.720		39.261	0.008
S15(2)a	WR	18.998	0.022	15.689	0.018	39.143	
S16(1)	WR	19.044		15.753		39.370	0.044
S17(1)a	WR	19.025	0.006	15.722	0.006	39.252	
S17(2)b	WR	18.929	0.001	15.606	0.0008	38.8613	0.021
S18(1)a	WR	18.901	0.002	15.585	0.001	38.796	0.002
S18(1)b	WR	18.949	0.0008	15.622	0.0008	38.9139	0.005
S19(1)a	WR	19.088	0.071	15.780	0.059	39.400	0.002
S20	WR	19.070	0.004	15.655	0.003	39.068	0.147
S20	WR	19.089		15.687		39.185	0.01
S21(1)a	WR	19.024	0.024	15.646	0.02	39.022	
S21(1)a	WR	19.043		15.677		39.139	0.05
S21(1)b	WR	19.030	0.012	15.677	0.011	39.137	
S21(1)b	WR	19.049		15.709		39.254	0.026
S21(1)c	WR	18.972	0.001	15.614	0.0009	38.906	
S21(1)c	WR	19.035	0.008	15.668	0.007	39.094	0.002
S21(1)c	WR	19.054		15.700		39.212	0.019
S21(2)c	WR	19.125	0.138	15.763	0.109	39.327	
S21(2)d	WR	19.038	0.006	15.673	0.005	39.113	0.276
S21(2)d	WR	19.058		15.704		39.231	0.0145
S21(2)e	WR	18.980	0.0009	15.602	0.0008	38.869	
S21(2)f	WR	18.997	0.001	15.615	0.001	38.916	0.002
S21(2)f	WR	19.016		15.646		39.032	0.004
V1a	WR	18.987	0.002	15.614	0.002	38.911	

Continued

R 1a	WR	19.006		15.646		39.028	0.005
V1b	WR	19.020	0.05	15.647	0.041	39.021	
R 1b	WR	19.040		15.679		39.138	0.102
V1c	WR	19.032	0.003	15.677	0.004	39.111	
R 1c	WR	19.051		15.708		39.229	0.012
V2a	WR	19.096	0.09	15.740	0.079	39.272	
R 2b	WR	18.985		15.646		39.015	0.15
V2b	WR	18.966	0.001	15.615	0.001	38.898	
V3a	WR	18.965	0.002	15.593	0.002	38.852	0.003
R 3a	WR	18.984		15.625		38.969	0.005
V3b	WR	19.054	0.004	15.656	0.002	39.076	
R 3b	WR	19.073		15.688		39.193	0.01
V4	WR	18.989	0.002	15.652	0.002	39.015	
R 4	WR	19.008		15.683		39.132	0.006
V5	WR	19.234	0.2	15.897	0.164	39.622	
V6a	WR	18.935	0.001	15.586	0.001	38.799	0.42
R 6a	WR	18.954		15.617		38.915	0.003
V6b	WR	18.977	0.013	15.639	0.011	38.982	
R 6b	WR	18.996		15.670		39.099	0.028
V6c	WR	18.979	0.009	15.638	0.008	38.976	
R 6c	WR	18.998		15.669		39.093	0.023
V7	WR	19.190	0.199	15.812	0.163	39.402	
V7	WR	19.024	0.001	15.630	0.001	38.885	0.413
V8	WR	18.929	0.008	15.612	0.007	38.874	0.003
R 8	WR	18.948		15.643		38.991	0.017
V9a	WR	18.985	0.01	15.629	0.009	38.932	
R 9a	WR	19.004		15.661		39.049	0.022
V9b	WR	18.967	0.003	15.614	0.002	38.898	
R 9b	WR	18.986		15.645		39.015	0.008
V10	WR	19.101	0.076	15.677	0.062	39.134	
R 10	WR	19.120		15.709		39.252	0.152
V14	WR	19.005	0.008	15.602	0.007	38.894	
V14	WR	19.024		15.633		39.011	0.017
V18	WR	18.999	0.009	15.595	0.008	38.867	
V18	WR	19.018		15.627		38.984	0.02
V21	WR	18.968	0.004	15.633	0.003	38.953	
V21	WR	18.987		15.664		39.070	0.008
V23	WR	18.968	0.006	15.636	0.005	38.976	
V23	WR	18.970	0.001	15.635	0.0009	38.954	0.014

Continued

V23	WR	18.987		15.667		39.093	0.002
V30	WR	18.954	0.001	15.616	0.0008	38.900	
V34	WR	18.980	0.003	15.659	0.002	39.054	0.002
V35	WR	18.985	0.004	15.651	0.004	39.031	0.015
V35	WR	19.004		15.683		39.148	
V42	WR	18.952	0.002	15.621	0.001	38.915	0.004
V42	WR	19.013	0.018	15.683	0.016	39.119	0.049
V42	WR	19.032		15.714		39.236	
V46	WR	18.963	0.001	15.630	0.001	38.935	0.003
V46	WR	18.982		15.661		39.052	
V59	WR	19.030		15.724		39.279	
V64	WR	18.991	0.002	15.632	0.002	38.948	0.005
V84	WR	18.959	0.001	15.614	0.001	38.901	0.002
V84	WR	18.946	0.0008	15.604	0.0008	38.856	0.002
V84	WR	18.942	0.003	15.601	0.003	38.844	0.008
V94	WR	19.178		15.767		39.435	
V97	WR	19.036	0.002	15.615	0.002	38.950	0.05
V97	WR	19.036	0.003	15.616	0.002	38.951	0.006
V102	WR	18.979	0.001	15.628	0.001	38.936	0.003
V102	WR	19.050		15.717		39.228	
V102	WR	19.031	0.029	15.685	0.026	39.110	0.067
V110	WR	18.964	0.001	15.602	0.0009	38.851	0.003
V141	WR	19.056	0.001	15.640	0.001	39.032	0.003
V155	WR	18.964	0.001	15.602	0.0009	38.851	0.003
SCL1	WR	18.988	0.002	15.602	0.002	38.902	0.007
SCD1	WR	18.981	0.003	15.607	0.003	38.891	0.009
SCL1a	WR	19.008	0.003	15.618	0.003	38.955	0.012
SCL3	WR	19.023	0.005	15.628	0.005	39.019	0.015
SCL4	WR	18.993	0.002	15.621	0.002	38.965	0.008
SCL5	WR	18.989	0.002	15.617	0.002	38.959	0.004
SCL6	WR	18.989	0.002	15.642	0.001	39.033	0.004
SCD2#1	WR	19.077	0.003	15.604	0.002	38.975	0.007
S2(2)c	KSP	18.963	0.002	15.650	0.003	39.018	0.008
S3(3)6	KSP	18.943	0.003	15.632	0.002	38.965	0.006

this study were −1 ng. The Pb isotopic data have a total uncertainty of 0.1% (2 s).

4. Discussion

The Pb isotopic composition is presented from mainly the Somma-Vesuvius volcano and cover the eruption ages from Somma caldera activity [<39 Ka (age of the Campanian Ignimbrite)] until the last vulcanian effusive eruption of 1944 AD (**Table 3**, [12], references therein). Then, a representative sample collection of the Campi Fle-

Table 2. Pb isotopic composition of a representative suite of volcanic rocks from Campi Flegrei District (CF), Roccamonfina (RM), Campi Flegrei Breccia Museo (CFb), Ignimbrite Campana (ICB, sanidine and whole rocks: ALT, MTF, SFC, Ve, Sa, Mo, MP), Somma caldera (SCL, SCD), Ventotene xenoliths (Vt).

Samples ID		Petrography	AGE	Lithotype	Pb206/ Pb204	2SE(M)	Pb207/ Pb204	2SE(M)	Pb208/ Pb204	2SE(M)
RM 1	Whole rock	Leuc-theph	1.5 - 0.3 MA	Lava	18.866	0.011	15.749	0.009	39.268	0.026
RM 1	Separate	Ksp			18.739	0.001	15.612	0.001	38.762	0.003
RM 3	Whole rock	K-Basalt	0.3 MA	Lava	18.943	0.006	15.617	0.005	38.968	0.016
RM 3'	Whole rock				19.167	0.004	15.683	0.003	39.209	0.01
RM 5	Whole rock	K-Basalt	0.3 MA	Lava	18.827	0.003	15.684	0.003	39.048	0.009
RM 6	Whole rock	K-Basalt	0.3 MA	Lava	18.839	0.003	15.680	0.003	39.039	0.009
RM 7	Whole rock	Leuc-tephr	1.5 - 0.3 MA	Lava	18.716	0.004	15.605	0.003	38.784	0.008
RM 7	Separate	Ksp			18.749	0.002	15.608	0.001	38.794	0.003
RM 8	Whole rock	K-basalt	0.3 MA?	Lava	19.119	0.002	15.677	0.002	39.177	0.005
RM 10	Whole rock	Latite	0.3 MA	Spatter cone?	19.093	0.002	15.678	0.002	39.173	0.008
RM 12	Whole rock	Trachibasalt	0.3 MA?	lava	18.884	0.003	15.687	0.007	39.080	0.018
CF X	Whole rock	K-Basalt		lava	19.201	0.0009	15.630	0.0007	39.116	0.002
CF 1	Whole rock	Trachibasalt	>40 ky BP	Scoria	19.032	0.004	15.620	0.002	38.948	0.008
CF 2	Whole rock	Trachibasalt	40 - 17 ky BP	Scoria	19.126	0.0006	15.615	0.0005	39.002	0.006
CF 3	Whole rock	Trachibasalt	17,000 y BP	Scoria	18.970	0.001	15.593	0.001	38.837	0.003
CF 5	Whole rock	Latite	?	Scoria	18.971	0.002	15.628	0.001	38.950	0.004
CF 6	Whole rock	Latite	14,000 y BP	Scoria	19.012	0.003	15.647	0.003	39.042	0.009
CF 7	Whole rock	Trachyte	10,000 y BP	Pomice	18.963	0.0007	15.666	0.0006	38.909	0.002
CF 8	Whole rock	Latite	40 - 10 ky BP	Pomice	18.989	0.002	15.638	0.002	38.990	0.007
CF 9	Whole rock	Latite	10 - 4 ky BP	Pomice	18.922	0.002	15.650	0.003	38.965	0.006
CF 10	Whole rock	Trachibasalt	8 - 5 ky BP	Pomice	18.936	0.001	15.580	0.0009	38.798	0.002
CF 10										
CFb 1	Whole rock	Basalt		Lava	18.974	0.002	15.684	0.002	39.082	0.008
CFb 2	Whole rock	Basalt		Lava	18.953	0.002	15.609	0.001	38.855	0.004
CFb 1	Ksp	Basalt			19.044	0.002	15.626	0.002	38.934	0.005
CFb 2	Ksp	Basalt			19.133	0.002	15.615	0.001	39.026	0.004
CFb 3	Ksp	Leuc-tephr.			19.277	0.001	15.659	0.0009	39.211	0.003
CFb 4	Ksp	Leuc-tephr.			19.241	0.002	15.641	0.001	39.138	0.004
ICB 1	Separate	Sanidine	37 - 33 ky BP		19.085	0.002	15.616	0.002	39.011	0.004
ICB 2	Separate	Sanidine	37 - 33 ky BP		19.159	0.003	15.695	0.004	39.266	0.014
ICB 3	Separate	Sanidine	37 - 33 ky BP		19.136	0.005	15.663	0.003	39.179	0.008
ICB 4	Separate	Sanidine	37 - 33 ky BP		19.136	0.005	15.663	0.003	39.061	0.003
ICB 5	Separate	Sanidine	37 - 33 ky BP		19.102	0.001	15.635	0.001	39.064	0.004
ICB HB6a	Separate	Sanidine	37 - 33 ky BP		19.112	0.001	15.649	0.001	39.118	0.005
ICB HB6b	Separate	Sanidine	37 - 33 ky BP		19.114	0.0007	15.642	0.0005	39.085	0.001
ICB HB7a	Separate	Sanidine	37 - 33 ky BP		19.122	0.0007	15.627	0.0006	39.049	0.001
ICB 8	Separate	Sanidine	37 - 33 ky BP		19.023	0.003	15.629	0.002	39.044	0.006
ICB 9	Separate	Sanidine	37 - 33 ky BP		19.128	0.0009	15.635	0.0007	39.078	0.002
ICB 9sec	Separate	Sanidine	37 - 33 ky BP		19.150	0.007	15.678	0.006	39.226	0.006
ICB 10	Separate	Sanidine	37 - 33 ky BP		19.133	0.0007	15.650	0.0006	39.122	0.001
ICB 11	Separate	Sanidine	37 - 33 ky BP		19.093	0.0009	15.625	0.0009	39.026	0.003
ICB 12	Separate	Sanidine	37 - 33 ky BP		19.108	0.0009	15.623	0.0008	39.046	0.002
ICB 13	Separate	Sanidine	37 - 33 ky BP		19.106	0.001	15.625	0.001	39.037	0.003

Continued

ICB 13sec	Separate	Sanidine	37 - 33 ky BP		19.118	0.0009	15.637	0.0008	39.076	0.002
ICB 14	Separate	Sanidine	37 - 33 ky BP		19.097	0.0008	15.621	0.0006	39.020	0.002
ICB 15	Separate	Sanidine	37 - 33 ky BP		19.095	0.006	15.620	0.005	39.024	0.012
ALT 1	Separate	Sanidine	37 - 33 ky BP		19.108	0.001	15.631	0.0008	39.056	0.002
ALT 2	Separate	Sanidine	37 - 33 ky BP		19.147	0.0007	15.670	0.0006	39.190	0.002
ALT 3	Separate	Sanidine	37 - 33 ky BP		19.115	0.0009	15.642	0.0009	39.090	0.003
ALT 4	Separate	Sanidine	37 - 33 ky BP		19.103	0.0006	15.629	0.0004	39.047	0.001
Ponti Rossi	Separate	Sanidine	37 - 33 ky BP		19.095	0.001	15.634	0.0007	39.055	0.002
MTF 1	Separate	Sanidine	37 - 33 ky BP		19.118	0.0006	15.642	0.0005	39.090	0.001
Pian Sorren.	Separate	Sanidine	37 - 33 ky BP		19.128	0.0007	15.633	0.0006	39.070	0.002
SFC 1a	Separate	Sanidine	37 - 33 ky BP		19.094	0.0006	15.631	0.0006	39.045	0.002
SFC 2	Separate	Sanidine	37 - 33 ky BP		19.109	0.0008	15.630	0.0008	39.051	0.002
Ve 1	Separate	Sanidine	37 - 33 ky BP		19.121	0.0005	15.628	0.0004	39.054	0.0009
Sa 1b	Separate	Sanidine	37 - 33 ky BP		19.112	0.0007	15.625	0.0006	39.038	0.001
Mo 1	Separate	Sanidine	37 - 33 ky BP		19.083	0.001	15.602	0.001	38.961	0.004
Mo 2	Separate	Sanidine	37 - 33 ky BP		19.106	0.0009	15.632	0.0007	39.053	0.002
MP 1	Separate	Sanidine	37 - 33 ky BP		19.144	0.001	15.657	0.001	39.151	0.003
MP 1	Separate	Sanidine	37 - 33 ky BP		19.154	0.0008	15.668	0.0007	39.185	0.002
MP 2a	Separate	Sanidine	37 - 33 ky BP		19.120	0.0008	15.626	0.0006	39.049	0.002
MP 2b	Separate	Sanidine	37 - 33 ky BP		19.109	0.001	15.635	0.0008	39.067	0.002
MPI-WB	whole rock		37 - 33 ky BP		19.137	0.001	15.651	0.001	39.133	0.003
VE-1-WB	Whole rock		37 - 33 ky BP		19.166	0.003	15.671	0.003	39.194	0.008
ALT-1-WB	Whole rock		37 - 33 ky BP		19.113	0.002	15.639	0.002	39.080	0.007
Sa 1a-WB	Whole rock		37 - 33 ky BP		19.072	0.003	15.617	0.002	39.067	0.007
Sa 1b-WB	Whole rock		37 - 33 ky BP		19.132	0.0004	15.652	0.0003	39.129	0.0009
ICB 9-WB	Whole rock		37 - 33 ky BP		19.148	0.001	15.656	0.001	39.151	0.005
SCL 1	Whole rock		35 - 25 ky BP	Lava	18.988	0.002	15.602	0.002	38.902	0.007
SCL 1a	Whole rock		35 - 25 ky BP		19.008	0.003	15.618	0.003	38.955	0.012
SCL 3	Whole rock		35 - 25 ky BP		19.023	0.005	15.628	0.005	39.019	0.015
SCL 4	Whole rock		35 - 25 ky BP	Lava	18.993	0.002	15.621	0.002	38.965	0.008
SCL 5	Whole rock		35 - 25 ky BP		18.989	0.002	15.617	0.002	38.959	0.004
SCL 6	Whole rock		35 - 25 ky BP		18.989	0.002	15.642	0.001	39.033	0.004
SCD #2-1	Whole rock		S.Cal. Dykes		19.077	0.003	15.604	0.002	38.975	0.003
Vt 1	Whole rock	Xenlith.			18.815	0.005	15.622	0.005	38.802	0.012
Vt 2	Whole rock	Xenlith.			18.538	0.007	15.603	0.006	38.506	0.019
Vt 3b	whole rock	Xenlith.			18.835	0.003	15.633	0.003	38.810	0.007
Vt 4	Whole rock	Xenolith.			18.757	0.001	15.637	0.001	38.857	0.003
Vt 4	Ksp	Xenolith.			18.765	0.001	15.647	0.001	38.888	0.003
Vt 5a	Whole rock	Xenlith.			18.742	0.002	15.623	0.001	38.810	0.003
Vt 5a	Ksp	Xenolith.			18.753	0.0008	15.629	0.0007	38.832	0.002
Vt 5b	Ksp	Xenolith.			18.737	0.002	15.621	0.002	38.804	0.004
Vt 6	Whole rock	Xenolith.			18.742	0.002	15.653	0.002	38.873	0.005

grei Volcanic District (Campi Flegrei, Procida and Ischia) is also presented. A detailed sampling especially for the separate sanidine very much present in the products of this eruption and several representative whole rocks (age of Campanian Ignimbrite eruption: 39 Ka, [13], **Figure 2**) of the Campanian Ignimbrite eruption and several representative analyses of Roccamonfina volcano [3] and Ventotene xenoliths [14] are also presented. The $^{207}Pb/^{204}Pb$ versus $^{206}Pb/^{204}Pb$ diagram is presented with all the above data and the following end members

[MORB [15] [16], Hercynian basement-Calabrian crust [17] [18], all the data worldwide of the shallow sediments and GLOSS (Global Sediment Subducting [19], Plank and Langmuir, 1998), Archean upper crust [16] (**Figure 3**)]. From the Pb-Pb diagram, I envisage that the all Campanian Volcanic Province is formed by three

Table 3. Eruption, age, and explosive tipology of Plinian and interplinian events in the last 25 ky.

Formation	Age	Type of activity	Magmatic groups	Dispersion direction	Volume (km^3)
Codola	25 ka BP	Plinian	I group	S-E	1.4
Post-Codola	25 - 17 ka BP	Strombolian and effusive	I group		
Sarno	17 ka BP	Plinian	I group	E	4.4 - 6
Post-Sarno	17 - 16 ka BP	Strombolian and effusive	I group		
Novelle-Seggiari-Bosco	15 - 14 ka BP	Plinian	I group	N-NE	1.5
Ottaviano	8 ka BP	Plinian	II group	E-NE	2.4
Avellino	3800 BP	Plinian	II group	E-NE	2.5
Protohistorical	3800 - 2700 BP	Vulcanian and strombolian	II group		
Pompei AD 79	79 AD	Plinian	III group	E-SE	~4
Ancient historical	79 - 203 AD	Vulcanian, strombolian and effusive	III group		
Pollena AD 472	472 AD	Plinian	III group	N-NE	1.2
Medieval	472 - 1139 AD	Vulcanian, strombolian and effusive	III group		
1631	1631 AD	Plinian	III group	N-NE	1.1
1631 - 1944	1631 - 1944 AD	Vulcanian, strombolian and effusive	III group		

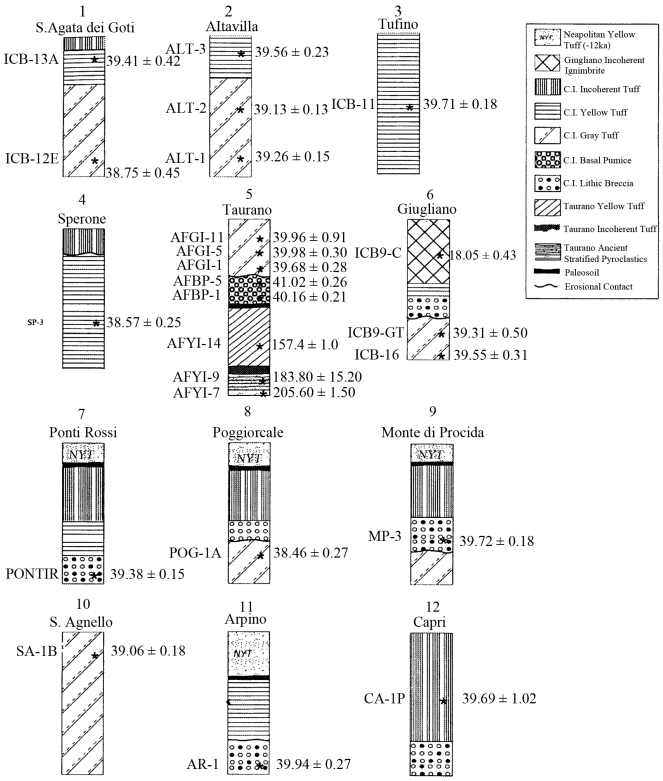

Figure 2. Schematic stratigraphic columns of the Campanian Ignimbrites. Ages are ka and are based on incremental-heating $^{40}Ar/^{39}Ar$ analyses of pure sanidine mineral separates (modified from [13]).

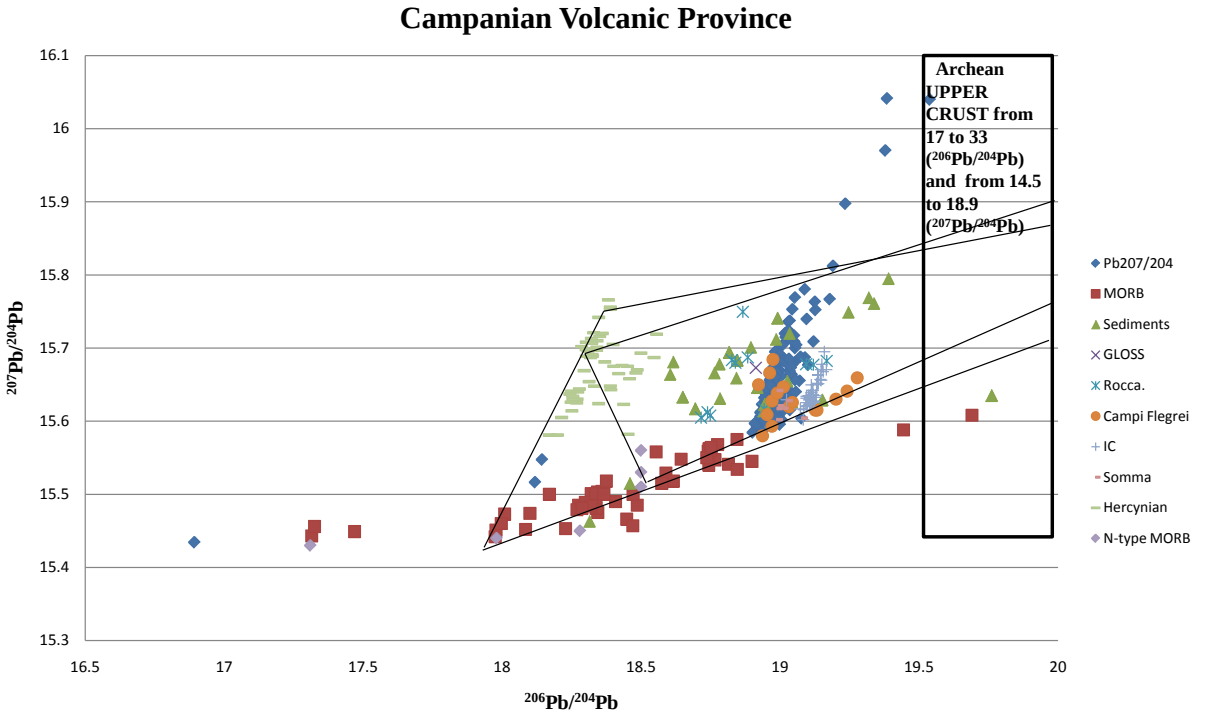

Figure 3. The $^{207}Pb/^{204}Pb$ versus $^{206}Pb/^{204}Pb$ diagram is presented with all the above data and the following end members [MORB [15] [16], Hercynian basement-Calabrian crust [17] [18], all the data worldwide of the shallow sediments and GLOSS (Global Sediment Subducting [19], Archean upper crust [16])].

end-menbers: 1) MORB, 2) Hercynian basement, 3) upper crust. This can be computed as I show with different styles of mixing duo to the large range of the end members. Anyhow, the result and interpretation does not change much. The model that I develop is that these volcanic products are produced by signatures of old arching upper crust and then assimilated with the Hercynian basement. Finally, I can also state that the recent sediments [19] are an average between the Hercynian component and the Archean upper crust as can be suggested by the past plate tectonic and the rock cycles.

5. Conclusion

Finally, I can say that the Campanian volcanic products are produced by a MORB component that has been contaminated by a series of upper crust component [20]. Anyhow, I can assume that the distinctive isotopic trend has also been influenced by an Archean upper crust. The magma has also undergone to storage and melting of a Hercynian component as testified by the presence of this kind of basement below the Campanian Volcanic Province. This model has been called deep and hot intrusion zone by [5]. In addition, I state that the GLOSS of [19] are a mixing of the Archean upper crust and Hercynian basement as in rock cycle operating.

Acknowledgements

The Pb isotope data have been produced in the laboratories of USGS, Reston, VA, USA. Thanks to Robert Ayuso to have always hosted me during my PhD. Thanks to the patience of Benedetto De Vivo as tutor during my PhD (1994-1999). Thanks to Chris Hawkesworth for an early review.

References

[1] Paone, A. (2006) The Geochemical Evolution of Somma-Vesuvius Volcano. *Mineralogy and Petrology*, **87**, 53-80. http://dx.doi.org/10.1007/s00710-005-0103-7

[2] Pappalardo, L., Piochi, M., D'Antonio, M., Civetta, L. and Petrini, R. (2002) Evidence for Multistage Magmatic Evolution during the Past 60 kyr at Campi Flegrei (Italy) Deduced from Sr, Nd, and Pb Isotope Data. *Journal of Petroleum*,

43, 1415-1434. http://dx.doi.org/10.1093/petrology/43.8.1415

[3] Paone, A. (2004) Evidence of Crustal Contamination, Sediment, and Fluid Components in the Campanian Volcanic Rocks. *Journal of Volcanology and Geothermal Research*, **138**, 1-26. http://dx.doi.org/10.1093/petrology/43.8.1415

[4] Paone, A. (2013) Petrogenesis of Trachyte and Rhyolite Magmatism on Ponza Island (Italy) and Its Relationship to the Campanian Magmatism. *Journal of Volcanology and Geothermal Research*, **267**, 15-29. http://dx.doi.org/10.1016/j.jvolgeores.2013.09.008

[5] Annen, C. and Sparks, R.S.J. (2002) Effects of Repetitive Emplacement of Basaltic Intrusions on Thermal Evolution and Melt Generation in the Deep Crust. Earth Planet. *Science Letters*, **203**, 937-955. http://dx.doi.org/10.1016/S0012-821X(02)00929-9

[6] Annen, C., Blundy, J.D. and Sparks, R.S.J. (2006) The Genesis of Intermediate and Silicic Magmasin Deep Crustal Hot Zones. *Journal of Petrology*, **47**, 505-539. http://dx.doi.org/10.1093/petrology/egi084

[7] D'Antonio, M., Civetta, L. and Di Girolamo, P. (1999) Mantle Source Heterogeneity in the Campanian Region (South Italy) as Inferred from Geochemical and Isotopic Features of Mafic Volcanic Rocks with Shoshonitic Affinity. *Mineralogy and Petrology*, **67**, 163-192. http://dx.doi.org/10.1007/BF01161520

[8] Scrocca, D., Doglioni, C. and Innocenti, F. (2003) Constraints for an Interpretation of the Italian Geodynamics: A Review. *Memorie descrittive della carta geologica d'Italia Servizio geologico d'Italia*, **62**, 15-46.

[9] Doe, B.R. (1970) Lead Isotopes. Minerals, Rocks and Inorganic Materials. Monograph Series of Theoretical and Experimental Studies 3. Springer, Berlin, 143.

[10] Faure, G. and Mensing, T.M. (2004) Isotopes: Principles and Applications. John Wiley and Sons, Hoboken, 897.

[11] Dickin, A.P. (2005) Radiogenic Isotope Geology. 2nd Edition, Cambridge University Press, Cambridge, 509. http://dx.doi.org/10.1017/CBO9781139165150

[12] Picarelli, L., Evangelista, A., Rolandi, G., Paone, A., Nicotera, M., Olivares, L., Scotto di Santolo, A., Lampitiello, S. and Rolandi, M. (2006) Mechanical Properties and Behaviour of Pyroclastic Soils in Campania Region. *Proceedings of the* 2*nd International Workshop on Characterisation and Engineering Properties of Natural Soils*, Singapore, 29 November-1 December 2006, 2331-2384.

[13] De Vivo, B., Rolandi, G., Gans, P.B., Calvert, A., Bohrson, B.A., Spera, F.J. and Belkin, H.E. (2001) New Constraints on the Pyroclastic Eruptive History of the Campanian Volcanic Plain (Italy). *Mineralogy and Petrology*, **73**, 47-65. http://dx.doi.org/10.1007/s007100170010

[14] De Vivo, B., Torok, K., Ayuso, R.A., Lima, A. and Lirer, L. (1995) Fluid Inclusion Evidence for Magmatic Silicate/Saline/CO_2 Immiscibility and Geochemistry of Alkaline Xenoliths from Ventotene Island, Italy. *Geochimica et Cosmochimica Acta*, **59**, 2941-2953. http://dx.doi.org/10.1016/0016-7037(95)00186-7

[15] Ito, E., White, W.M. and Gopel, C. (1987) The O, Sr, Nd and Pb Isotope Geochemistry of MORB. *Chemical Geology*, **62**, 157-176. http://dx.doi.org/10.1016/0009-2541(87)90083-0

[16] Rollinsson, H.G. (1993) Using Geochemical Data: Evaluation, Presentation, Interpretation. Pearson Education Limited, Harlow, 380.

[17] Rottura, A., Del Moro, A., Pinarelli, L., Petrini, R., Peccerillo, A., Caggianelli, G.M. and Piccarretta, G. (1991) Relationships between Intermediate and Acidic Rocks in Orogenic Granitoid Suites: Petrological, Geochemical and Isotopic (Sr, Nd, Pb) Data from Capo Vaticano (Southern Calabria, Italy). *Chemical Geology*, **92**, 153-176. http://dx.doi.org/10.1016/0009-2541(91)90054-U

[18] Ayuso, R.A., Messina, A., De Vivo, B., Russo, S., Woodruff, L.G., Sutter, J.F. and Belkin, H.E. (1994) Geochemistry and Argon Thermochronology of the Variscan Sila Batholith, Southern Italy: Source Rocks and Magma Evolution. *Contributions to Mineralogy and Petrology*, **117**, 87-109. http://dx.doi.org/10.1007/BF00307732

[19] Plank, T. and Langmuir, C.H. (1998) The Composition of Subducting Sediment and Its Consequences for the Crust and Mantle. *Chemical Geology*, **145**, 325-394. http://dx.doi.org/10.1016/S0009-2541(97)00150-2

[20] Paone, A. (2013) A Review of Carbonatite Occurrences in Italy and Evaluation of Origins. *Open Journal of Geology*, **3**, 66-82. http://dx.doi.org/10.4236/ojg.2013.32011

Open Journal of Geology, 2015, 5, 13-27
Published Online January 2015 in SciRes. http://www.scirp.org/journal/ojg
http://dx.doi.org/10.4236/ojg.2015.51002

Mineralogical Characteristics of Garnet in Garnet Mica Schist and Its Tectonic Significance in the Tongbai Section of the Shangdan Fault Zone

Shenglian Ren*, Chuanzhong Song, Jiahao Li

School of Resources and Environmental Engineering, Hefei University of Technology, Hefei, China
Email: *ren_lotus@126.com, czsong69@163.com, lijiahaohappy@sina.com

Received 29 December 2014; accepted 22 January 2015; published 26 January 2015

Copyright © 2015 by authors and Scientific Research Publishing Inc.
This work is licensed under the Creative Commons Attribution International License (CC BY).
http://creativecommons.org/licenses/by/4.0/
Open Access

Abstract

Studies on the metamorphism and deformation conditions of rocks in the suture zone are good ways to discuss the orogenic process and mechanism. The microstructure and ultramicrostructure features of minerals are true embodiment of formation environment of the orogenic belt. Based on the study of microstructure, ultramicrostructure deformation characteristic and compositional zonation of garnets in garnets-mica schists in the Tongbai mountain, east section of the Shangdan fault zone, the results show that the three types of garnets have suffered various states of plastic deformation. The dynamic recrystallization of garnets is due to the subgrain growth and boundary migration. The dislocations are mainly free dislocation and dislocation walls. The free dislocation density $\rho = 6.14 \times 10^8/cm^2$, and dislocation movement are mainly slips; slip planes are 1/2 <111> {110} and <100> {001}. Garnet microprobe analysis shows that it belongs to almandine, and reflects it has undergone epidote-amphibolite to amphibolite facies metamorphism. Compositional zonation of garnet shows that the rocks had experienced progressive metamorphism. First metamorphic environment was continuous temperature-pressure and in mid-term there were two non-synchronous transient cooling and decompression processes, and it finally underwent decompression and warming process of the thermal relaxation environment. The formation condition of garnet-mica schist is estimated: T = 562˚C - 617˚C, and P = 0.77 - 1.02 GPa. The differential stress is 0.511 GPa and strain rate is 4.97536×10^{-10} m/s. After systemic analysis, a conclusion is drawn that the plastic deformation mode, deformation mechanism and formation environment of garnets are closely related to the formation and development of the Shangdan fault zone. It truly reflects that the Shangdan fault zone, as the suture zone of Yangtze and north China plate, has been subjected to early medium-grade metamorphism. With the continuous compression after the collision, the left-lateral shearing happened and caused the formation of high density dislocations

*Corresponding author.

How to cite this paper: Ren, S.L., Song, C.Z. and Li, J.H. (2015) Mineralogical Characteristics of Garnet in Garnet Mica Schist and Its Tectonic Significance in the Tongbai Section of the Shangdan Fault Zone. *Open Journal of Geology*, **5**, 13-27.
http://dx.doi.org/10.4236/ojg.2015.51002

and subgrains of the garnets; finally the plastic deformation happened and the bulging recrystallization formed in the period of heat relaxation had a relative low stress.

Keywords

The Tongbai Area, The Shangdan Fault Zone, Metamorphism and Deformation, Compositional Zonation of Garnet, Dislocation

1. Introduction

The Central Orogenic Belt is one of the key areas where the Eastern Paleo-Tethyan ocean closed and consequently the adjacent blocks and terranes collided. The belt comprises Qilian mountain, Kunlun mountain and Songpan mountain in the west which converge to Qinling, Tongbai and Dabie mountains in the east. This belt is attributed to the intracontinental orogeny in the late Cenozoic [1]. Qinling, Tongbai and Dabie mountains of the central orogen are the result of subduction of the Yangtze plate and its collision with the North China plate. The Shangdan fault zone as the suture zone of the two plates is recognized by many geologists [1] [2]. Study of the fault zone is helpful to reveal the mechanism, process and tectonic environment of the deep subduction and the regional metamorphism involved. Metamorphism study and deformation structural analysis of rocks within the suture are the key.

2. Geology Setting

The Shangdan fault in the Tongbai area of the suture zone is an important tectonic boundary. To its north and South are respectively the Northern Tongbai and the Southern Tongbai, corresponding to southern Qinling and Northern Qinling in the Qinling Mountains area. Shangdan fault is well exposed only to the north of Tongbai mountain and west of Xingyang due to the subsequent tectonic destruction after it developed. It is about 1 - 3 km wide and up to 45 km long in east-west direction. Various ductile deformation structures are observed in the field. Mylonitic foliation generally dips toward south with dip mostly at more than 60˚. Lineation plunges to 280˚ - 340˚ with plunge of 15˚ - 30˚. A variety of kinematic indicators suggest that Shangdan fault zone in Tongbai is a large sinistral ductile shear zone.

To the south of Shangdan fault zone is Tongbai gneiss uplift belt. To the north are Hongyi River-Luozhuang eclogite belt and Maopo-Hu Jiazhai volcano rock belt. Tongbai gneiss uplift belt is also known as the Tongbai complex. The rock is mainly composed of granitic gneiss, black mafic inclusions and marble lens. Schistosity dips to the southwest. The dip angle is 30˚ - 40˚. Rocks in Hongyi River-Luozhuang eclogite belt are garnet mica schists, glaucophane schist, amphibolite schists and different components of blastomylonite [3]. Schistosity dips to northeast. Dip angle is in the range of 25˚ - 35˚. A large amount of veins, lenticular or layered eclogite or garnet amphibolite are exposed in the Hongyi River, Luozhuang temple and goddess temple. They are a few hundred centimeters in size. Its occurrence is consistent with eclogite in Dabie area. Hongyi River-Luozhuang eclogite belt is in contact with the Maopo-Hu Jiazhai volcano rock belt at a normal fault. The rocks in Shangdan fault zone are felsic schist and gneiss, containing a small amount of marble lens and amphibolite interlayers [4]. The samples were collected from the southwest side of Xinyang City (**Figure 1**). The lithology is garnet mica schist whose composition is consistent with Hongyi River-Luozhuang eclogite outside of the fault zone, and it is interpreted as derived from deformed equivalence to the eclogite [5]. In this study, we present the mineralogical study and the formation environment of garnet, and use them to reveal the tectonic evolution of Shangdan fault zone in Tongbai area.

3. The Deformation Characteristics of Garnet Mica Schist

3.1. Mineral Assemblages of Garnet Mica Schist

The mineral assemblage of the garnet mica schist is quartz, muscovite, biotite, garnet, epidote and a small amount of feldspar. The garnet mica schist has a porphyroblastic structure and porphyroblasts are garnets. The

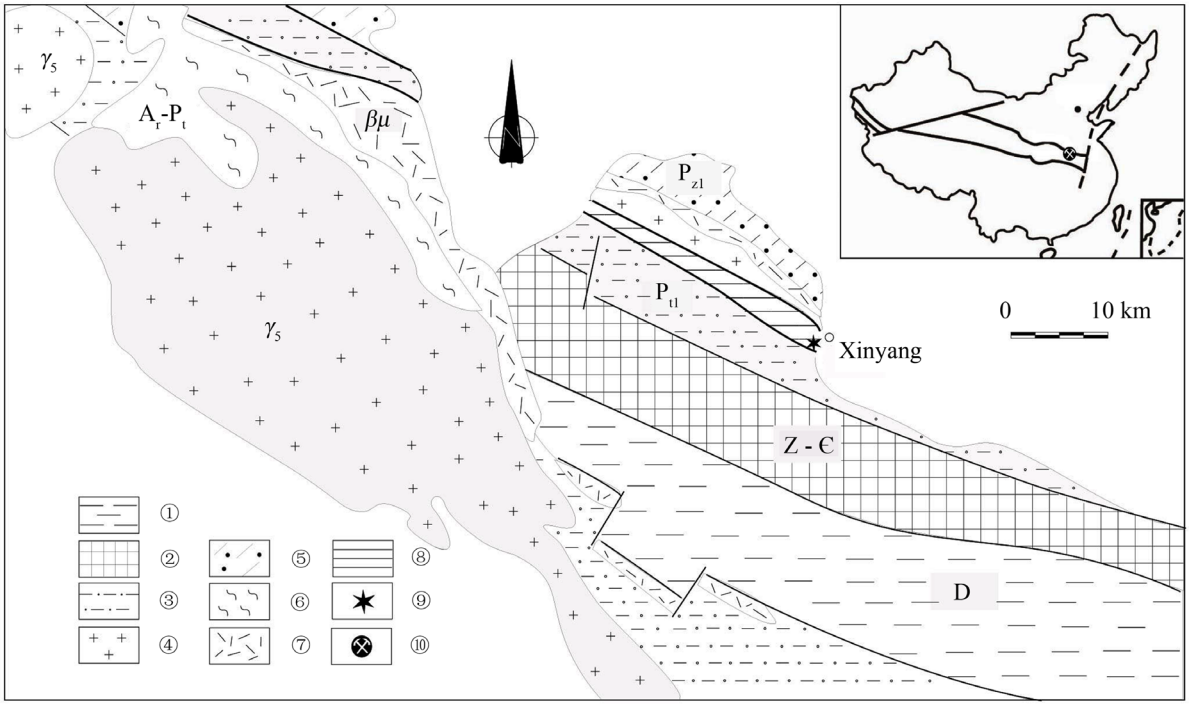

Figure 1. Geological map of work area and sampling location. 1. Devonian metasandstone; 2. Greenschist of Foziling group; 3. Tongbai gneiss uplift belt; 4. Yanshanian volcanic belt of Maopo-Hujiazhai; 5. Basic rock of Erlangping; 6. Granitic gneiss; 7. Indosinian basic rock; 8. Eclogite belt of Hongyihe-Luozhuang; 9. Sample location; 10. Work area.

matrix is quartz, muscovite, biotite, epidote and plagioclase. Matrix has fine crystalloblastic or micro lepidoblastic texture, and schistose structure. Rocks show strong ductile deformation. Quartz occurs as ribbons with sweeping undulose extinction and aspect ratios of more than 10:1 (**Figure 2(a)**). Static recrystallization is visible in quart ribbons and is interpreted as having formed in later tectonic thermal relaxation. Muscovites occur at both sides of garnet and gather in the garnet pressure shadows. The muscovites are elongated and have a preferred orientation. Biotite and Muscovite coexist and together define the foliation. Small biotites occur in garnet pressure shadows or at the edge of garnet. Epidote show the shape of datestone in the matrix (**Figure 2(b)**). Some occur in garnet pressure shadows. Matrix possess fine crystalloblastic or micro lepidoblastic texture. In the XZ surface, the "S-C" structure is obvious.

3.2. The Deformation Characteristics of Garnets

According to the mineralogical characteristics of garnet porphyroblasts in the sample, garnet can be divided into three categories. Garnets (Gt_1) in the first category are rounded or dodecahedral in shape. Inclusions are abundant in the garnets and define concentric rings which are clearly visible under the microscope. Large garnet crystals have 3 - 5 zones separated by the rings (**Figure 2(c)**). The sizes of the garnets vary between 1 - 0.5 mm. Garnet porphyroblasts is surrounded by foliations in the matrix, and pressure shadow is visible. These porphyroblasts and the pressure shadows together have monoclinic shape symmetry, and are "σ" type mantled clasts. The asymmetry indicates sinistral shearing. The garnets (Gt_2) in the second category are with helicitic structure. Inclusions of quartz and mica align to define the internal foliation within gargets. The internal foliations form spiral patterns (**Figure 2(d)**), and these garnets are "snowball" garnets. The foliations can be traced continuously from the internal foliation in the garnets to the external foliations outside of the garnets in the matrix. This characteristic suggests that these garnets grew while it was rotating during the non-coaxial deformation [6]. Garnets (Gt_3) in the third category are small and subrounded to rounded in shape, similar to the garnets in the first category but with fewer or no rings defined by inclusions.

All garnet clasts developed before the end of deformation, which is suggested by that all garnets are associated with pressure shadows and are wrapped by late foliations. Micro-structure study reveals that garnets in the

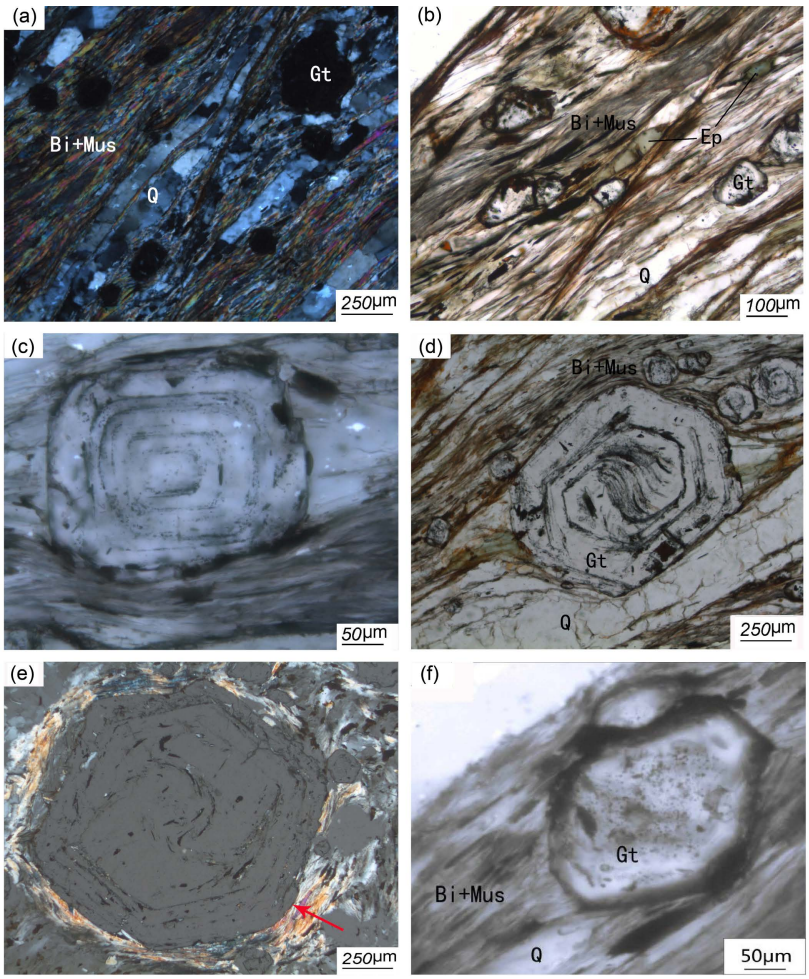

Figure 2. Micrographs of garnet-mica schist. (a) Quartz vein, epidote and garnet (Gt_3) in the spectrum; (b) Type I garnet (Gt_1); (c) (d) Type II garnet (Gt_2); (e) (f) Dynamic recrystallization of garnets and "core-mantle structure".

three different categories grew at different stages of deformation. Gt_2 garnets have inner cores with spiral-shaped inclusions and outer edges with concentric-ringed inclusions. Gt_1 and Gt_3 garnets do not have inner core but contain inclusions with patterns similar to those in the outer edge of Gt_1 garnets. Dynamic recrystallized garnets occur at the margins of Gt_1 and Gt_2, and their shapes are similar to Gt_3 garnets (**Figure 2(e)** and **Figure 2(f)**). The similarities between Gt_1, Gt_3, and outer part of G_3 garnets suggest that they might grow during the same sage. The inner core of Gt_2 grew at an early stage and Gt_1, Gt_3, and outer part of G_3 garnets grew at a later stage. Garnets of all the samples are syntectonic with the suture zone deformation.

Although garnets in each category have their own characteristics, all garnets are syntectonic garnets. This can be interpreted with decomposition of deformation [7]. Bell noted that inhomogeneity of the geological structure of native or heterogeneity of deformation, resulting in deformation of rock inhomogeneity. In progressive deformation process, rock deformation can be decomposed into progressive sheer deformation component and progressive shortened deformation component, and usually layered silicate minerals like mica minerals occupy sheer deformation domain, as mica class mineral; in shortened deformation domain there is usually granular phenocryst minerals. When it grows it is vulnerable to shear deformation domain on both sides, the neighboring mostly flaky mineral, and such metacrystal typically grow larger. Porphyroblasts is generally not easy to nucleation grow in deformation component parts where the mica mineral gathered, however, under certain conditions when strain rate is very small, growth of phenocrysts is in priority within the deformation zone where mica minerals gathered, because in this band there is not only the material elements required to build the phenocrysts, and also it is at a relatively static environment [8]. Phenocrysts particles in these two growth environments, the for-

mer is lager and the latter particles smaller and easy to produce “s-shaped” or “snowball-like” structure. Therefore, they are products at different stages in the process of deformation, belonging to the same tectonic origin.

4. Characteristics of Garnet Composition

4.1. Crystal Chemistry of Garnet

Garnet chemical equation can be written as $A_3B_2[SiO_4]_3$, where A represents bivalent cation Ca^{2+}, Mn^{2+}, Fe^{2+}, Mg^{2+}, Na, K, and Y, etc., and B Al^{3+}, Fe^{3+}, Cr^{3+}, V^{3+}, Ti^{4+}, and Zr^{4+}, etc. One of the most important crystal chemistry of garnet is their crystal structures are complex. Most garnet is body-centered cubic crystal system with space group of Ia3d. Isolated $[SiO_4]$ tetrahedra in crystal structure is connected by coordination polyhedron $[BO_6]$ which is composed of cations of category B (Al^{3+}, Fe^{3+}, Cr^{3+}, and V^{3+} etc.). In the course of the formation of distortion large cubic space, it is occupied by class A cation, forming distortion cubic coordination polyhedron $[AlO_8]$.

It is well known that temperature and pressure conditions have an impact on cation coordination number of the crystal structure, such as: warming causes cationic coordination number decreases, booster increases the coordination number. Cationic coordination number and composition reflect the forming environment of garnets. Typically, the coordination number of A class cationic of Garnet (Ca^{2+}, Mn^{2+}, Fe^{2+}, and Mg^{2+}) is 8, due to the radius of the Ca^{2+} 0.112 nm, eight times of coordination is appropriate, without too much pressure. Therefore, the formation of grossular andradite, do not need too much pressure, mostly formed in the contact metamorphic band where pressure is not big, while ionic radius of Mn^{2+} (0.096 nm), Fe^{2+} (0.092 nm), Mg^{2+} (0.089 nm) is smaller, and it decrease follow this order. In general they tend to enjoy six times coordination, it needs pressure increased conditions if they enjoy eight times coordination, so spessartine generates in low-level regional metamorphic conditions with pressure slightly high, while almandine generates in intermediate regional metamorphic conditions with higher pressure, and pyrope only generates in conditions of very high pressure, as eclogite, and kimberlite [9]. Therefore, temperature-pressure conditions of the formation of garnet can be estimated by use of content and variety of Ca, Mn, Fe, Mg components of garnet.

4.2. The Composition of Garnets in the Garnet Mica Schist and Their Significance

This section presents electron microprobe analysis results for the three types of garnets (**Tables 1-3**). The analy-

Table 1. The compositions of garnet for sample 09-2914-1.

Composition	Center edge									
Na_2O	0.06	0.00	0.04	0.07	0.08	0.03	0.06	0.00	0.03	0.02
FeO	28.50	28.86	29.49	30.48	30.82	31.92	32.27	31.57	32.71	33.58
K_2O	0.00	0.01	0.00	0.00	0.01	0.00	0.01	0.00	0.00	0.02
SiO_2	37.07	37.23	37.03	37.07	36.23	36.92	36.91	37.17	36.83	38.07
MnO	5.98	5.89	5.34	5.01	3.95	4.00	3.22	2.71	1.69	1.58
MgO	1.32	1.28	1.40	1.45	1.45	1.60	1.58	1.77	2.01	2.09
CaO	4.78	4.75	4.52	4.14	5.14	3.62	4.11	4.56	4.46	3.91
Al_2O_3	20.90	21.00	20.90	21.02	21.60	20.98	21.15	21.11	21.18	21.39
Total	98.61	99.10	98.73	99.26	99.40	99.08	99.37	98.90	98.94	100.64
Na	0.02	0.00	0.01	0.02	0.03	0.01	0.02	0.00	0.01	0.01
Fe	3.89	3.92	4.02	4.14	4.19	4.35	4.38	4.29	4.45	4.47
K	0.00	0.00	0.00	0.00	0.00	0.00	0.00	0.00	0.00	0.00
Si	6.05	6.05	6.04	6.02	5.89	6.01	5.99	6.03	5.98	6.06
Mn	0.83	0.81	0.74	0.69	0.54	0.55	0.44	0.37	0.23	0.21
Mg	0.32	0.31	0.34	0.35	0.35	0.39	0.38	0.43	0.49	0.49
Ca	0.84	0.83	0.79	0.72	0.90	0.63	0.72	0.79	0.78	0.67
Al	4.02	4.02	4.02	4.03	4.14	4.03	4.05	4.04	4.06	4.02
Total	15.96	16.00	15.97	15.98	16.09	15.98	16.04	15.95	16.00	15.93

Table 2. The compositions of garnet for sample 09-2914-4.

Composition	Center edge									
Na_2O	0.07	0.02	0.02	0.07	0.02	0.00	0.02	0.02	0.00	0.00
FeO	27.80	28.31	28.70	28.72	30.14	29.61	30.52	31.16	29.39	33.04
K_2O	0.00	0.00	0.00	0.00	0.00	0.01	0.02	0.00	0.00	0.02
SiO_2	36.99	36.91	37.04	36.94	36.94	36.66	37.01	36.92	35.63	37.18
MnO	8.02	7.66	7.65	7.25	6.92	6.65	5.35	3.43	2.22	0.90
MgO	1.27	1.28	1.33	1.36	1.47	1.45	1.50	1.64	1.68	2.09
CaO	3.81	3.98	3.94	4.06	4.14	3.99	3.86	3.91	5.02	5.28
Al_2O_3	20.81	21.07	21.24	21.17	21.17	20.97	21.19	20.90	21.24	21.38
Total	98.78	99.27	99.95	99.57	100.82	99.34	99.47	97.98	95.21	99.92
Na	0.02	0.01	0.01	0.02	0.01	0.00	0.01	0.01	0.00	0.00
Fe	3.80	3.86	3.88	3.90	4.06	4.04	4.14	4.27	4.12	4.44
K	0.00	0.00	0.00	0.00	0.00	0.00	0.00	0.00	0.00	0.00
Si	6.05	6.01	5.99	5.99	5.95	5.98	6.00	6.05	5.97	5.97
Mn	1.11	1.06	1.05	1.00	0.94	0.92	0.73	0.48	0.31	0.12
Mg	0.31	0.31	0.32	0.33	0.35	0.35	0.36	0.40	0.42	0.50
Ca	0.67	0.69	0.68	0.71	0.71	0.70	0.67	0.69	0.90	0.91
Al	4.01	4.04	4.05	4.05	4.02	4.03	4.05	4.04	4.20	4.05
Total	15.96	16.01	16.00	15.99	16.05	16.01	15.98	15.93	15.95	16.01

Table 3. The compositions of matrix garnet.

Composition	Center edge		
Na_2O	0.05	0.03	0.05
FeO	30.49	31.83	31.92
K_2O	0.03	0.02	0.03
SiO_2	37.54	37.32	37.17
MnO	0.77	0.93	1.16
MgO	2.05	2.30	2.09
CaO	7.61	5.43	5.38
Al_2O_3	21.13	21.35	21.43
Total	99.71	99.19	99.28
Na	0.02	0.01	0.02
Fe	4.08	4.29	4.30
K	0.01	0.00	0.01
Si	6.01	6.01	5.99
Mn	0.10	0.13	0.16
Mg	0.49	0.55	0.50
Ca	1.31	0.94	0.93
Al	3.99	4.05	4.07
Total	16.02	15.97	16.02

sis was conducted in the electron probe laboratory in Guangzhou Institute of Geochemistry, Chinese Academy of Sciences, using the electron probe microscope (instrument model JEOL, JXA-8100, analysis conditions for the acceleration voltage is 15.0 kv, beam 2×10^{-8} A, beam 1 μm). PRZ is adopted for error correction method.

The garnet compositions are projected in the Coleman garnet classification diagram (Coleman, 1965). Garnet composition data are all plotted in almandine zone (**Figure 3**), and the average composition is that almandine is about 67% - 87%, calcium aluminium garnet approximately 13% - 24%, and pyrope approximately 2% - 12%. Gt_1 garnets comprise 66.83% - 76.42% almandine, 3.63% - 13.82% spessartine, 10.65% - 14.08% essonite, and 5.27 - 8.46 pyrope. From the center to the margin, the molecular content of almandine garnet stone and pyrope

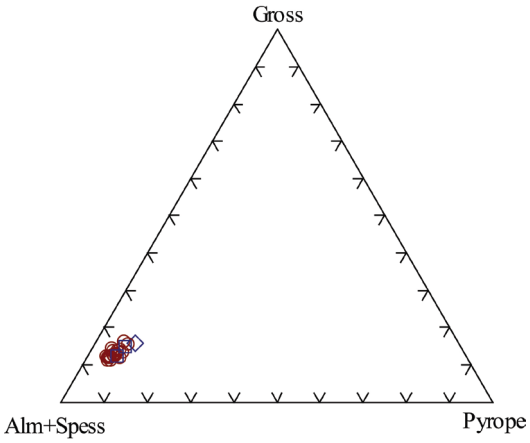

Figure 3. The triangle plot for garnet compositions.

gradually increase, and the spessartine content gradually decrease, and essonite content increase first and then decrease (**Figure 5(a)**). Gt_1 has the typical characteristics of compositional zoning pattern developed in progressive metamorphism with elevated temperature and pressure. Gt_2 garnets are composed of 65.11% - 74.34% almandine, 2.04% - 17.83% pyrope, 11.35% - 15.67% essonite, and 5.23% - 8.40% pyrope. From the center to the margin, the almandine and essonite contents first increase and then decrease, and the spessartine content first decreases and then increases, and pyrope content increases all the way (**Figure 5(b)**). Compared with the Gt_1 garnet, compositional zoning pattern of Gt_2 garnets are more complicated, and it reflects the complex metamorphic reaction. Gt_3 garnets have a higher percentage of pyrope than the Gt_1 and Gt_2 garnets (**Figure 5(c)**). Garnet compositions of the three categories suggest that the rock intermediate grade regional metamorphism [10].

In Nadi garnet composition and metamorphic zone diagram (**Figure 4**), although all plotted either within or close to the kyanite zone, garnets in each category spread out or are concentrated at different areas. All Gt_1 and Gt_3 garnets are plotted in the kyanite zone while some Gt_2 garnets are plotted in the garnet zone. Gt_1 garnets spread out in the whole kyanite zone but Gt_3 garnets are plotted on the part of zone that is close to the sillimanite zone. These differences suggest that Gt_1 garnets grew slightly earlier than Gt_3 garnets but later than G_2 garnets. Projection results showed that all garnets grew in epidote-amphibolite facies to amphibolite facies metamorphism.

Electron microprobe analysis of the garnet shows the zoning within garnets is growth zoning which can truly reflect the growth environment. The average composition of garnet is 67% - 87% almandine, 13% - 24% essonite, and 2% - 12% pyrope. In Coleman garnet classification diagram, all garnets fall into the almandine zone.

Probe data show that garnets studied here have distinct compositional zoning. Garnet composition zones are generally formed by growth causes or diffusion causes. Growth zoning is caused by various factors such as material supply in the process of garnet growth at different stages. Diffusion zoning is a result of intergranular diffusion in the crystal growth process or of ion exchange reaction or pure conversion reaction after garnet stopped growing [11]. Growth zoning is characterized by increased Mg percentage and decreased Mn percentage with temperature increase [12], and especially by bell-shaped Mn profile. The garnet probe data of our samples show typical characteristics of the growth zoning, and zones in the garnets are growth zones. These garnets can be used to estimate the temperature of its environment.

Studies of the garnet composition zoning in the literature show that MgO, FeO, MnO, and CaO contents vary with metamorphic p-t conditions. As metamorphic temperature rises, MgO content increases and MnO content decreases. CaO content increases gently with pressure [13]. With deepened metamorphic strength, percentages of Fe^{2+}, and Mg^{2+} in garnet increase, but Mn^{2+} decreases. This is because Mn^{2+} in spessartine crystal lattice is not stable and is replaced by Fe^{2+} to become almandine; coordination number of a class cation Ca^{2+}, and Mn^{2+}, and Fe^{2+}, and Mg^{2+} in pomegranate stone is 8, Ca^{2+} Ca^{2+} have the largest radius, Ca^{2+} present eight time coordination and need not pressure, booster will makes the coordination number increase. So, with the deterioration the content of Ca^{2+} is only slightly up [14].

$X_{Gt,Mg}$, $X_{Gt,Fe}$, $X_{Gt,Mn}$, and $X_{Gt,Ca}$ values of garnet in metamorphic rocks are under the influence of the chemical

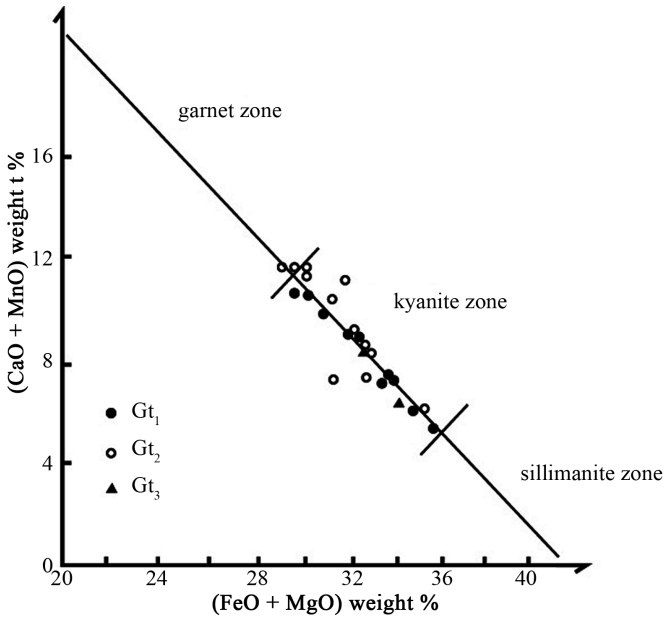

Figure 4. Diagram showing the relationship between compositional of garnets and metamorphic belt.

composition of the host rock, and under the control of metamorphic temperature, under conditions of chemical composition, their change reflects changes in metamorphic environment [15]. For any garnets in this study, composition of the core differs from that of the rim, but this composition difference for each of the three categories of garnets has their own characteristics.

For Gt_1 garnets (09-2914-1) the difference is distinctive. From the center to the margin, X_{Mg} and X_{Fe} increase monotonically and X_{Mn} decreases monotonically. X_{Ca} decreases near the core and increases in the middle and then gradually decreases toward the margin (**Figure 5(a)**).

For Gt_2 garnets (09-2914-4), the difference is minor. From the center to the margin, X_{Mg}, X_{Fe}, X_{Mn}, and X_{Ca} show different patterns (**Figure 5(b)**). X_{Mg} increases monotonically. X_{Fe} increases first and then falls. X_{Mn} decreases first and then increases. X_{Ca} increases gently first and then decreases. For Gt_3 garnets, the difference is minor. X_{Mg} continues to increase, X_{Fe} waves rising and falling, X_{Mn} to decline slowly and then rapidly decline; X_{Ca} is wave-like rising (**Figure 5(c)**).

The patterns of the profile plots of $X_{Gt,Mg}$, $X_{Gt,Fe}$, $X_{Gt,Mn}$, $X_{Gt,Ca}$ of the above three types of garnet suggest an overall progressive metamorphism with complex metamorphic history. Garnet core grew gradually in an environment with increasing temperature and pressure. The plot pattern for the outer edge indicates that the pressure increased rapidly first with elevated temperature and then the temperature decreased dramatically, followed first by dramatical decrease of pressure and then rapid rise of temperature and gentle increase of pressure. Combines samples collection points location it can be analysed the growth environment for pomegranate stone of the samples is: rock first in regional metamorphism, produces progressive metamorphic; after that local pressure increased and led to uplift producing temprature cooling down, as pressure continues to increase and fault zone formed, part stress was released leading pressure declined; finally garnet regrow in the thermal relaxation environmental warming slightly pressurized (part of euhedral garnet also reflects the characteristics of static recrystallization). The whole process of garnet growth correspond to the different periods of orogeny, garnet core growth has characteristics of large fold-nappe in early orogenic phaseand tectonic stacking with regional low-temperature dynamic metamorphism. Mantle and edge growth has characteristics of strike-slip, decrease, uplifted tectonic mechanisms and processes shown by the principal orogenic compressional, with progressive metamorphism, granitization and progressive deformation. Garnet did not reflect metamorphism of power degradation of late orogenic process [16].

All in all, composition characteristics of three categories of garnets imply that the garnets grew in a progressive metamorphism and that they did not undergo retrogressive metamorphism. This research coincides with Yang Weiran, who, in his view: “the beihuaiyang tectonic belt was subjected to greenschist facies metamor-

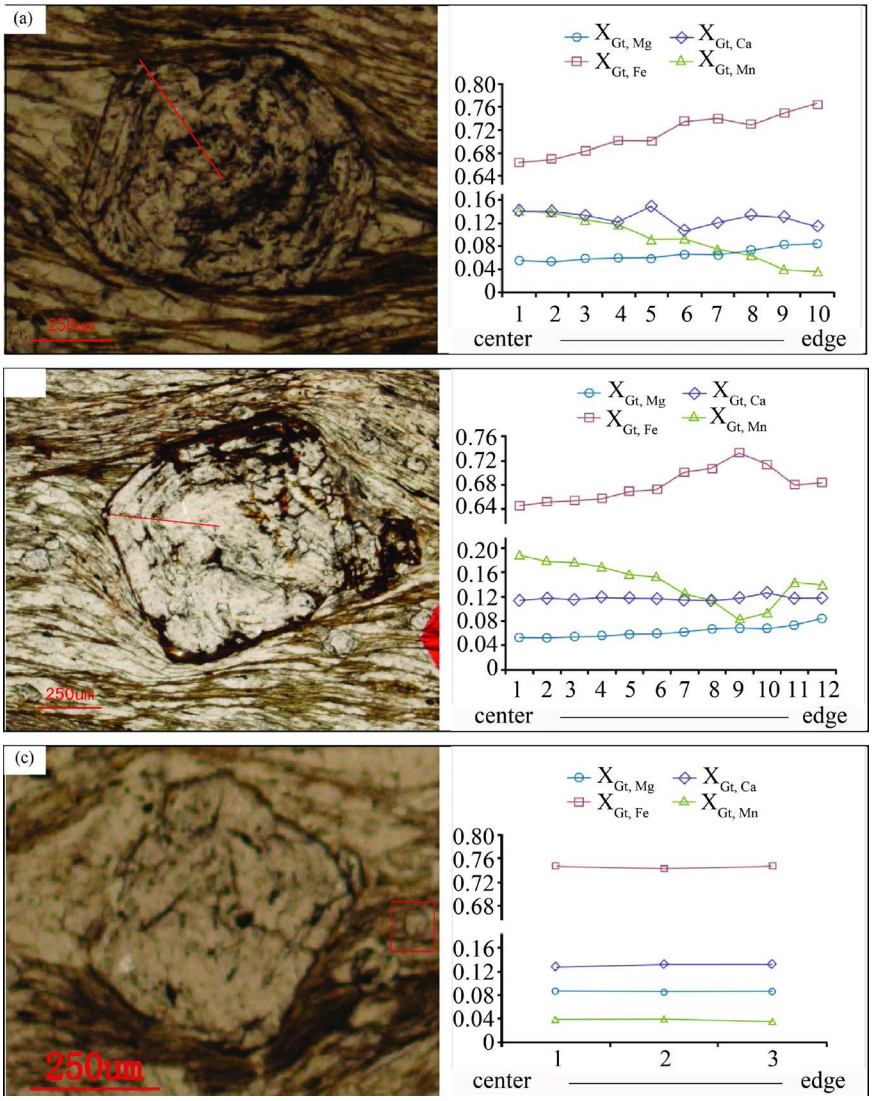

Figure 5. Compositional profile of garnet. (a) Microprobe analysis profile of Gt_1 garnet (09-2914-1); (b) Microprobe analysis profile of Gt_2 garnet (09-2914-4); (c) Microprobe analysis profile of Gt_3 garnet (the mineral matrix). Thereinto, $X_{Gt. Fe} = Fe/(Mg + Fe^{2+} + Mn + Ca)$; $X_{Gt. Mn} = Mn/(Mg + Fe^{2+} + Mn + Ca)$; $X_{Gt. Mg} = Mg/(Mg + Fe^{2+} + Mn + Ca)$; $X_{Gt. Ca} = Ca/(Mg + Fe^{2+} + Mn + Ca)$.

phism, and metamorphic is deep along the fault zone, in the local area of garnet mica schist there are high-pressure eclogite facies metamorphism". As the main rock unit in of the tectonic zone and the protolith of the surrounding country rock of the eclogites, garnet mica schist, experienced the same tectonic phases as the eclogites. These tectonic phases contributed to and left footprints in the composition zoning of the garnets in this study.

5. Ultrastructure Deformation Characteristics of Garnet

In order to study the phenomenon of the micro rheology of garnet and rheological mechanisms, the author carried on detailed Transmission Electron Microscope (TEM) analysis of the garnet samples in the physical and chemical center in China University of Science and Technology. Analysis shows that there is a link between the characteristics of dislocations with the garnets and tectonic history of the fault zone. Free dislocations, dislocation walls, small amounts of dislocation arcs, and circular spots formed by water molecules were observed.

Free dislocations are mostly long and straight mainly in two directions, along one of which dislocations dominate (**Figure 6(a)**). This is the direction in which it is easy for garnet dislocation slip to take place. In complex crystals, surface most prone to sliding is generally parallel to the weakest chemical bonds between the lattice planes. For garnet, the sliding surface is 1/2 <111> {110} and the other slip systems is <100> the {001}, because 1/2 <111> <100> is two short sets of crystal lattice dislocations Borges vector, keys in the other direction is weak and liable to undermine formation of slip surface. Dislocation bowing turns a small amount, and radian is smaller. Dislocation wall is clear and tidy, it is obvious that both sets of slip surface on the flat sliding surface parallel to the dislocation in the met and formed equally spaced, and are the result of dislocation slip intersect (**Figures 6(b)-(d)**). But with cold-finished condition observed diffuse tangles of dislocations wall is significantly different in Asia and grained low dislocation density, intracellular corrugated matting, lattice of notes bent, dislocation climb should be moved under the control of slip was Weertman creep [17]. Mechanism is the relatively high temperature, low stress and strain, roughly comparable to the middle and lower crust temperature and pressure environment. Because the two groups of varying degrees of slip surface slip, so crystal cell morphology is not isometric, but a bit long ellipsoidal, consistent with Gt_3 and Sub grain recrystallization grain morphology under microscopy.

For garnet, dislocation slip and climb can only occur as the leading mechanisms of plastic deformation when T is >0.8 Tm (about 900˚C) [18]. From the picture in **Figure 6**, you can see the contrast of small circular spots (**Figure 6(b)**, **Figure 6(c)**, **Figure 6(e)** and **Figure 6(f)**), and this should be water molecules in garnet repeatedly reported in recent years, dislocation line around water molecules is little or no. Because of water molecular diffusion under high temperatures accelerate, priority mission of occupying space and room in the lattice forming small water molecules, water molecules gathered again through diffusion and form larger molecules of water. Therefore, water molecules are the result of static recovery at high temperature [19]. These two different structural features illustrate garnet had undergone a certain high temperature static recrystallization of the restore process after experiencing a strong dislocation slip deformation [20].

Dynamic recrystallization is the result of reduced dislocation density in the deformed crystal. Recrystalliza-

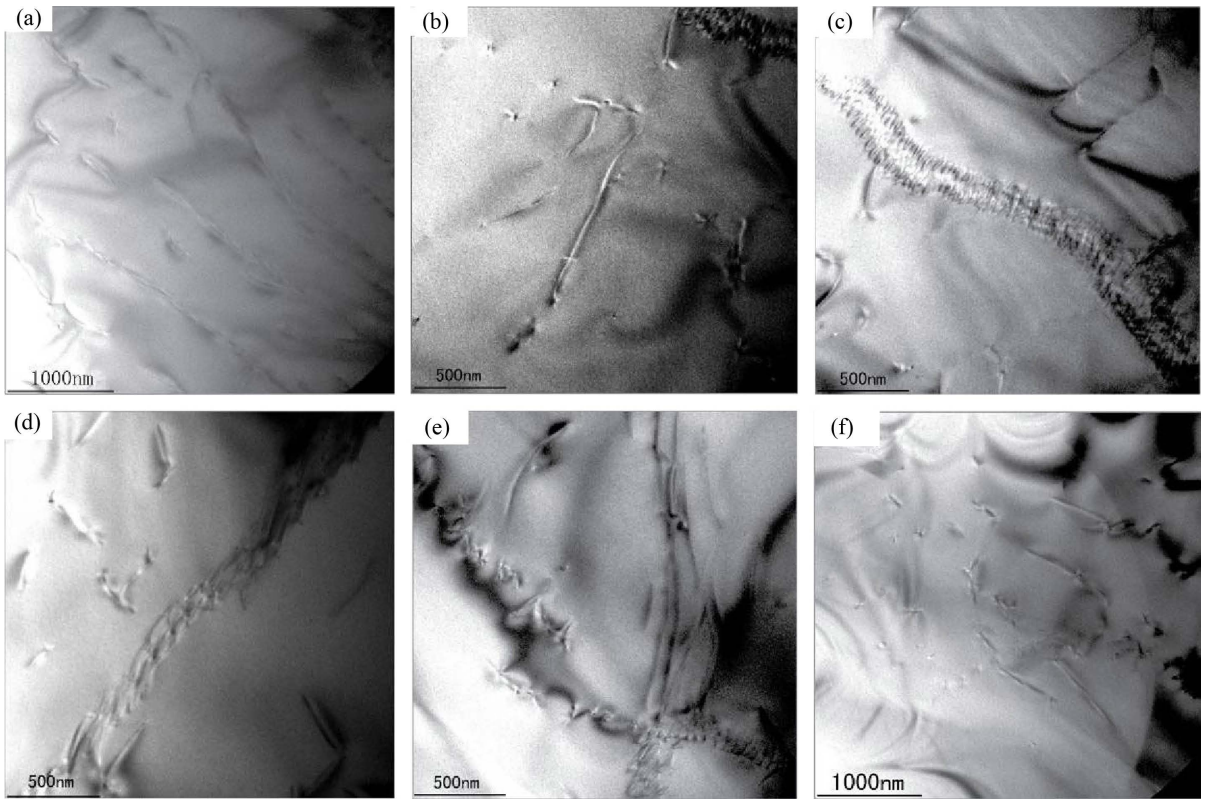

Figure 6. TEM photos of garnet (Gt_3). (a) Straight free dislocation; (b) Free dislocation and dislocation bow; (c) (d) Dislocation wall; (e) Dislocation bow and dislocation wall; (f) Free dislocation and the water molecules.

tion contain nucleation and growth process of new crystal, in this process, High dislocation density of the particulate material is transferred to the boundary of the low dislocation density in the crystal lattice, the particles of weak deformation increases while the particles of strong deformation decreases. Its formation mechanism is when crystals are subjected to external stresses, due to uneven internal structure, the stress concentration generated in the secondary phase particles at the grain boundaries and, in the crystal of the type stored plastic strain energy will cause free energy difference and produces a driving force, under the action of this force, the rotation of the two mechanisms of strain in the grain boundaries and grain protuberances Guinea grains recrystallized grains formed the core, and on the basis of this it grows to a new crystal and replace the old strain grain [21]. Intensity of crystallization (ratio of the new nucleus and residual strain of grain), is closely related to size and strain. Whereas the recrystallized grain size depends primarily on differences in deformation stress, so it's often used to calculate the differences in stress.

Dynamic recrystallization falls into three types: bulging recrystallization, subgrain rotation recrystallization and grain boundary migration recrystallization. Some of the samples show small garnets at the margin of and connected with the large garnet crystals, and these are the core-mantle structures at the early stage (**Figure 2(b)**, **Figure 2(d)**, **Figure 2(f)** and **Figure 2(e)**). They are the product of a bulging dynamic recrystallization.

In summary, the plastic deformation of garnet in the sample is formed by plastic deformation dominated with dislocation slip mechanism along with bulging dynamic recrystallization formed by protuberantia of strainied grain boundary. According to various microstructural features of garnet, it's convinced the plastic deformation of the sample is formed in medium and slightly higher temperature conditions.

6. The Rheological Parameters of Garnet and Rheological Parameters of Rock

By means of probe analysis on Garnet and Muscovite in rock and Garnet-Muscovite thermometer and phengite geobarometer the formation environment can be estimated. These garnets, developed compositional zoning in progressive metamorphism, and that their rims are in equilibrium with muscovite at a temperature of 562˚C - 617˚C [22]. Muscovite probe analysis datum are calculated based on 11 oxygen, Si atomic number ranges between 3.08 - 3.15, slightly larger than 3.0, but haven't reached ingredients of phengite [23]. Pressure is 0.77 - 1.02 GPa [22]. Conditions of temperature and pressure garnet suffered are consistent and with dislocation configuration under TEM observation and the metamorphism and deformation environment shown by the recrystallization form.

Particle size of Muscovite in garnet mica schist is small, 0.05 - 0.1 mm, schistose, in the matrix it is in interphase arrangement with biotite and distribution parallel to the schistosity. Porphyroblast garnet have obvious metamorphism zone, so its edge ingredients and garnet rim of muscovite composition was chosen to estimate peak metamorphic conditions. Muscovite microprobe analysis data are shown in **Table 4**, calculated by 11 oxygen crystal chemical formula, the change is 3.08 - 3.15 Si, Si cation is slightly larger than the number of muscovite in 3.0, but has not reached phengite ingredients. According to Garnet-Muscovite geological thermometer its equilibrium temperature is estimated as 562˚C - 617˚C, pressure is estimated as 0.77 - 1.02 GPa.

Dislocation density in most metals and minerals and the stress applied have the following relationship:

$$\sigma / 2\mu = \alpha\left(\rho b^2\right)^{1/k}$$

σ is the variance stress, μ is the shear modulus, α is material coefficient, ρ is the dislocation density, b is the Burgers vector, k is a constant.

Material factor is currently used in the calculation of differential stress of garnet and olivine. As material factor α varies with different minerals, therefore, Chen corrected garnet material coefficients compared with the calculated values of other minerals, and thought the outcome of calculating the difference in stress is more reasonable when $\alpha = 2.5$ [24].

12 TEM photos of samples are selected and free dislocation densities are measured an average of $\rho = 6.14 \times 10^8/\text{cm}^2$, by substituting ρ on the type differential stress of 0.511 GPa. Using Parrish wet quartz flow rate formula to calculate the strain rate.

$$\varepsilon\left(s^{-1}\right) = 4.4\times10^{-2} \times\left(\sigma\left(\text{MPa}\right)\right)^{2.6} \times\exp\left(-27778/T\left(\text{K}\right)\right)$$

Choose Garnet-Muscovite thermometer to calculate the average deformation temperature T = 89.5˚C, the

Table 4. The representative compositions for muscovite.

Si	3.15	3.13	3.08	3.15	3.08	3.10	3.12	3.11
Al^{IV}	2.71	2.72	2.68	2.74	2.71	2.67	2.73	2.74
Sum_T	5.86	5.85	5.77	5.88	5.79	5.76	5.86	5.85
Ti	0.02	0.02	0.02	0.02	0.02	0.02	0.02	0.02
Fe^2	0.10	0.10	0.27	0.09	0.23	0.24	0.11	0.12
Mn	0.00	0.00	0.00	0.00	0.00	0.00	0.00	0.00
Mg	0.07	0.07	0.06	0.06	0.07	0.08	0.06	0.06
Ca	0.00	0.00	0.01	0.00	0.01	0.00	0.01	0.00
Na	0.08	0.08	0.09	0.08	0.09	0.09	0.09	0.10
K	0.78	0.79	0.78	0.74	0.77	0.82	0.77	0.82
O	11.00	11.00	11.00	11.00	11.00	11.00	11.00	11.00
Fe_FeMg	0.60	0.57	0.81	0.61	0.78	0.76	0.64	0.66
Mg_FeMg	0.40	0.43	0.19	0.39	0.22	0.24	0.36	0.34

calculated strain rate 4.97536×10^{-10} $m \cdot s^{-1}$. Although moving dislocation and TEM observation of dislocation density has some differences, but the scope should also be an order of magnitude range so the results has some availability.

To further understand deformation state and deformation strength in the tectonic zone, Under the microscope, using the method of the length of the shaft [25], respectively, the XY plane, XZ and YZ plane surface, garnet and quartz of the rocks were conducted strain measurement, triaxial strain rate of garnet in garnet-mica schist in the eastern extension of Shangdan fault was calculated averaged X:Y:Z = 1.43:1.21:1, Flinn Coefficient of pomegranate stone k is 0.948 (**Figure 7**), showing garnet contingency mechanism should be a plane strain; Triaxial strain ratio of quartz is of average X:Y:Z = 77:6.19:1, and k value of quartz is 4.84 (**Figure 8**), shaft for single cigars-variant. Three axis strain ratio and Flinn coefficient of different mineral in one rock is obviously different, reflecting out this two species mineral of different strength, and on same deformation conditions strain acts are obviously different. In strong deformation domain in ductile shear belt, pomegranate stone and quartz together suffered tectonic deformation, due to their different hardness the strain they bear is not the same, quartz took most of the dependent variable, and garnet bear little strain, or as a rigid body it is only weak deformed or undeformed even under the strain. Their corresponding relations between deformation remains to be further researched.

7. Conclusions

Study of the structures of garnets within the Shangdan suture zone using the microscope, the TEM, and the electron microprobe enables us to reveal the characteristics and origin of these garnets and to use them to constrain the tectonic evolution of the Shandan suture zone which developed during the collision between North China plate and South China plate.

1) Garnets in all of the three categories underwent dynamic recrystallization. Gt_1 and Gt_2 garnets are equigranular, and ductile deformation occurs at the edge and is not as strong as G_3 garnets. Gt_3 garnets are small rounded elongated crystals. Dynamic recrystallized garnets of this category can be separated from the residual amorphous, and core-mantle structure is at the beginning.

2) Two main dislocations in garnet are free dislocations and dislocation wall, with small amounts of dislocation arc. Garnet dislocation motion is dominated by slip; slip surface is 1/2 <111> {110} and <100> {001}. Garnet experienced static recrystallization process after strong dislocation glide deformation, which shows that in early-to-mid term, the rock experienced a relatively strong stress and garnet formed high density of dislocations and subgrain. Finally in the thermal relaxed stage of relatively low stress bulge type recrystallization generated, bringing about plastic deformation and dynamic recrystallization of the garnet. And water molecules in garnets suggest that the garnets have experienced a certain high-temperature static recrystallization recovery process after

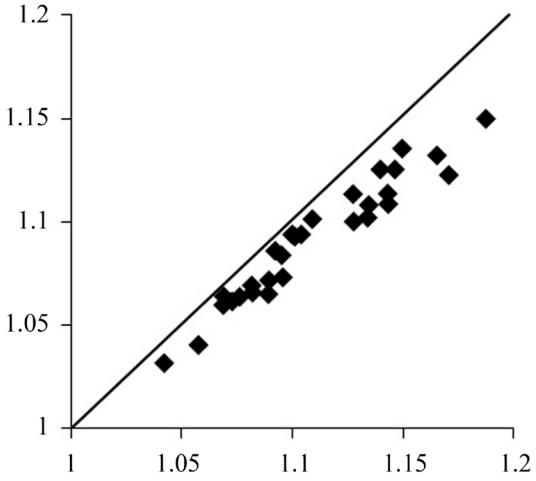

Figure 7. Flinn diagram of garnet finite strain.

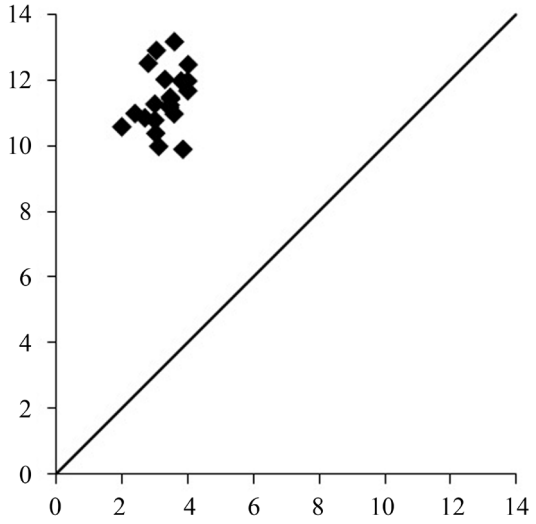

Figure 8. Flinn coefficient of quartz finite strain.

dislocation glide deformation.

3) Ompositional characteristics of garnets indicate the garnet mica schist has experienced progressive metamorphism. On Coleman garnet classification maps, garnets all fall onto the almandine zone, reflecting that the rock has gone through the intermediate regional metamorphism; on Nadi composition and metamorphic belt diagram, garnet rests primarily with kyanite zone with slightly garnet, showing that rock suffered the epidote amphibolite facies and amphibolite facies metamorphism.

4) According to geological thermometer of garnet-phengite, the temperature at which garnet mica schist developed is estimated to be 562˚C - 617˚C. The pressure calculated by phengite geobarmeter is 0.77 - 1.02 GPa. The average value of free dislocation density (ρ) is $6.14 \times 10^{8}/cm^{2}$. The differential stress is 0.511 GPa. Using Parrish wet quartz flow rate formula, the strain rate is calculated to be 4.97536×10^{-10} m·s^{-1}. The mean value of three-axis strain ratio of garnet X:Y:Z = 1.43:1.21:1, and the Flinn index of 0.948 implies plane-strain deformation of garnets. The triaxial strain ration of quartz X:Y:Z = 77:6.19:1. Flinn coefficient of quartz is 4.84.

Based on mineralogical study of garnet in garnet mica schist, the metamorphism and deformation environment of Shangdan suture zone in the Tongbai area is: in the early stage of collision of the Yangtze and north China plate, the suture zone went through intermediate grade regional metamorphism; with the collision continued, the left-lateral shearing happened and caused the formation of high-density dislocations and subgrains of the garnets, then the dynamic recrystallization was formed in the process of thermal relaxation and caused the

plastic deformation of garnets at last. So, deformation characteristics of microstructure and ultrastructure, and the composition zoning revealed formation, development and evolution of Shangdan suture zone in Tongbai area.

Acknowledgements

Financial support for this study was jointly provided by the National Natural Science Foundation of China (Grants: 41272213, 41072161).

References

[1] Zhang, G.W. and Liu, X.M. (1998) Some Remarks on China Central Orogenic System. *Earth Science*, **23**, 443-448. (In Chinese with English Abstract)

[2] Song, C.Z., Zhang, G.W., Ren, S.L., Li, J.H. and Huang, W.C. (2009) The Research on Deformation Features of Some Structural Zones in the Qinling-Dabieshan Orogenic Belt. *Journal of Northwest University* (*Natural Science Edition*) **39**, 368-380. (In Chinese with English Abstract)

[3] Liu, X.C., Lou, Y.X. and Dong, S.W. (2005) P-T-t Path of Low-Temperature Eclogites from the Tongbaishan Area. *Acta Petrologica Sinica*, **021**, 1081-1093. (In Chinese with English Abstract)

[4] Huang, S.Y. and Xu, B. (2006) Geometry, Kinematics and Evolution of the Tongbai Orogenic Belt. *Earth Science Frontiers* (*D Series*), **36**, 242-251. (In Chinese with English Abstract)

[5] Wei, C.J., Wu, Y.X., Ni, Y.Y., Chen, B. and Wang, S.G. (1999) The Characteristics of Eclogite and Its Geological Significance in Tongbai Area in Henan Province. *Chinese Science*, **44**, 1882-1885. (In Chinese with English Abstract)

[6] Bell, T.H. and Johnson, S.E. (1995) Porphyroblast Inclusion Trails: The Key to Orogenesis. *Journal of Metamorphic Geology*, **7**, 279-310. http://dx.doi.org/10.1111/j.1525-1314.1989.tb00598.x

[7] Bell, T.H. and Forde, A. (1995) On the Significance of Foliation Patterns Preserved around Folds by Mineral Overgrowth. *Tectonohysics*, **246**, 171-181. http://dx.doi.org/10.1016/0040-1951(94)00263-9

[8] Williams, M.L. (1994) Sigmoidal Inclusion Trails, Punctuated Fabric Development, and Interactions between Metamorphism and Deformation. *Journal of Metamorphic Geology*, **12**, 1-21. http://dx.doi.org/10.1111/j.1525-1314.1994.tb00001.x

[9] He, T.X. (1980) Metamorphic Petrology. Geological Publishing House, Beijing, 60-65. (In Chinese with English Abstract)

[10] Clarke, G.L., Aitchison, J.C. and Cluzel, D. (1997) Eclogites and Blueschists of Pam Penisula, NE New Caledonia: Are Appraisal. *Journal of Petrology*, **38**, 843-876. http://dx.doi.org/10.1093/petroj/38.7.843

[11] Spear, F.S. and Daniel, C.G. (2001) Diffusion Control of Garnet Growth, Harpswell Neck, Maine, USA. *Journal of Metamorphic Geology*, **19**, 179-195. http://dx.doi.org/10.1046/j.0263-4929.2000.00306.x

[12] Cygan, R.T. and Lasaga, A.G. (1985) Self-Diffusion of Magnesium in Garnet at 750 to 900˚C. *Science*, **285**, 328-350.

[13] Menzer, G. (1928) Die kristallstrktur der Granate. *Zeitschrift für Kristallographie*, **69**, 300-396.

[14] O'neill, B., Bass, J.D., Smyth, J.R. and Vaughan, M.T. (1989) Elasticity of Grossular-Pyrope-Almandine Garnet. *Journal of Geophysical Research*, **94**, 17819-17824. http://dx.doi.org/10.1029/JB094iB12p17819

[15] Chen, N.S. and Sun, M. (2003) Major- and Trace-Element Zoning in Metamorphic Garnets and Their Metamorphic Process Implications. *Earth Science Frontiers*, **10**, 315-320. (In Chinese with English Abstract)

[16] Ji, S.C. and Martignole, J. (1997) Fracturing of Garnet Crystals in Anisotropic Metamorphic Rocks during Uplift. *Journal of Structure Geology*, **19**, 603-620. http://dx.doi.org/10.1016/S0191-8141(97)00006-0

[17] Nicolas, A. and Poirier, J.P. (1976) Crystalline Plasticity and Solid State Flow in Metamorphic Rocks. John Wiley & Sons, New York.

[18] Voegele, V., Ando, J.I. and Cordier, P. (1998) Plastic Deformation of Silicate Garnets I High-Pressure Experiments. *Physics of the Earth and Planetary Interiors*, **108**, 305-318. http://dx.doi.org/10.1016/S0031-9201(98)00110-1

[19] Wang, Y.F. and Jin, Z.M. (2001) Diffusion Creep of Rocks and Its Implications. *Geological Science and Technology Information*, **20**, 5-10. (In Chinese with English Abstract)

[20] Brok, B.D. and Kruhl, J.H. (1996) Ductility of Garnet as an Indicator of Extremely High Temperature Deformation: Discussion. *Journal of Structural Geology*, **18**, 1369-1373. http://dx.doi.org/10.1016/S0191-8141(96)00064-8

[21] Prior, D.J., Wheeler, J. and Brndnker, F.E. (2000) Crystal Plasticity of Natural Garnet: New Microstructures Evidence. *Geology*, **28**, 1003-1006. http://dx.doi.org/10.1130/0091-7613(2000)28<1003:CPONGN>2.0.CO;2

[22] Ren, S.L., Song, C.Z., Lin, S.F., Zhang, H.R., Li, J.H., Tu, W.C., Zhang, H. and Zhang, J.J. (2011) Mineralogy Feature

and Tectonic Significance of Garnet from Garnet-Mica Schist at the West Section of Xinyang-Shucheng Fault Belt. *Chinese Journal of Geology*, **46**, 350-363. (In Chinese with English Abstract)

[23] Massonne, H.J. and Szpurka, Z. (1997) Thermodynamic Properties of White Micas on the Basis of High-Pressure Experiments in the Systems K_2O-MgO-Al_2O_3-H_2O and K_2O-FeO-Al_2O_3-SiO_2-H_2O. *Lithos*, **41**, 229-250. http://dx.doi.org/10.1016/S0024-4937(97)82014-2

[24] Chen, Y., Wei, C.J., Zhang, J.S. and Chu, H. (2005) Phase Equilibria of Mica-Schists and Gneisses in the HP-UHP Belt of Southern Dabie Shan. *Acta Petrologica Sinica*, **21**, 1657-1668. (In Chinese with English Abstract)

[25] Zheng, Y.D. and Chang, Z.Z. (1985) Finite Strain Measurement and Ductile Shear Zones. Geological Publishing House, Beijing, 188. (In Chinese with English Abstract)

Open Journal of Geology, 2015, 5, 28-37
Published Online January 2015 in SciRes. http://www.scirp.org/journal/ojg
http://dx.doi.org/10.4236/ojg.2015.51003

Temporal and Spatial Variations of Accommodation and Sediment Accumulation during Transgressive to Highstand Stages as Reconstructed from a Latest Pleistocene to Holocene Sequence in the Intra-Arc Osaka Basin, Japan

Fujio Masuda, Natsumi Itomoto

Department of Environmental System Sciences, Faculty of Science and Engineering, Doshisha University, Kyoto, Japan
Email: fmasuda@mail.doshisha.ac.jp

Received 29 December 2014; accepted 23 January 2015; published 26 January 2015

Copyright © 2015 by authors and Scientific Research Publishing Inc.
This work is licensed under the Creative Commons Attribution International License (CC BY).
http://creativecommons.org/licenses/by/4.0/
Open Access

Abstract

Temporal and spatial variations in accommodation (*i.e.*, paleo-water depth) and sediment accumulation (amount of deposition) in the intra-arc Osaka Basin, Japan, were reconstructed from the post-glacial transgression through the sea-level highstand, a total of 9000 years. At the beginning of the marine transgressive stage (about 11,000 cal y BP), paleo-water depths were shallow and the sediment accumulation was large. The area occupied by Osaka Bay gradually extended and sediment deposition decreased from 11,000 to 6000 cal y BP. During the period of maximum transgression (6000 - 5000 cal y BP), an inner bay, Kawachi Bay with a water depth of 5 - 10 m, was expanded in the inland eastern Osaka area, and paleo-water depths reached a maximum and depositional rates reached a minimum. During the subsequent highstand and small regression (about 5000 cal y BP to the present), however, deposition increased rapidly as a result of river delta and shoreline progradations. Regional differences were observed in accommodation and accumulation between the outer bay area and the inner bay area. During both the transgressive and regressive stages, deposition decreased in the inner bay area. In contrast, in the outer bay area and in the basin overall, deposition was high during the first part of the transgressive stage but it decreased during the maximum transgression, before reaching a maximum during the subsequent highstand and regression. During the regressive stage, fluvial delta progradation led to the forma-

How to cite this paper: Masuda, F. and Itomoto, N. (2015) Temporal and Spatial Variations of Accommodation and Sediment Accumulation during Transgressive to Highstand Stages as Reconstructed from a Latest Pleistocene to Holocene Sequence in the Intra-Arc Osaka Basin, Japan. *Open Journal of Geology*, **5**, 28-37. http://dx.doi.org/10.4236/ojg.2015.51003

tion of a thick sequence of delta body sediments. Sediment accumulation was 30% - 40% higher during the regressive stage than that during the transgressive stage.

Keywords

Accommodation, Holocene, Osaka Plain, Paleo-Depths, Sediment Accumulation, Sequence Stratigraphy

1. Introduction

Sequence stratigraphy is a relatively new geological paradigm that is used to classify sedimentary strata and clarify their formation history [1] [2]. Sequence stratigraphic methods have gained worldwide acceptance and have had a great impact on stratigraphic and sedimentological studies, including in Japan [3]. Sequence stratigraphy, however, was originally applied to long-buried strata for which a detailed chronology could not be established. Because of the lack of detailed chronological information, it has been difficult to discuss dynamically the formation of strata.

The uppermost Pleistocene to Holocene succession in Japanese coastal areas is the youngest depositional sequence for which ^{14}C ages have been determined with measurement error of less than 100 years [4]-[6]. Deposition of this sequence began at about 30 - 18 ka above the sequence boundary. During the long marine transgressive stage started from 11 ka, relative sea level rose about 50 m. Maximum transgression was reached at about 6000 - 5000 cal y BP. During the regression that followed the sea-level highstand (about 5000 cal y BP to the present), relative sea level decreased by about 3 m [7]-[9].

In this report, we propose a new method for analyzing sequence formation based on borehole data densely dated with many ^{14}C ages from the Osaka intra-arc basin. We examine temporal and spatial changes in paleowater depth, representing accommodation, and depositional amounts, representing sediment accumulation during these 9000 years, to clarify the youngest depositional sequence in this region.

2. Analytical Methods and Results

2.1. Borehole Sites and Areas

The Osaka Plain lies in an intra-arc basin in western Japan (**Figure 1**). In this study we used well-dated borehole

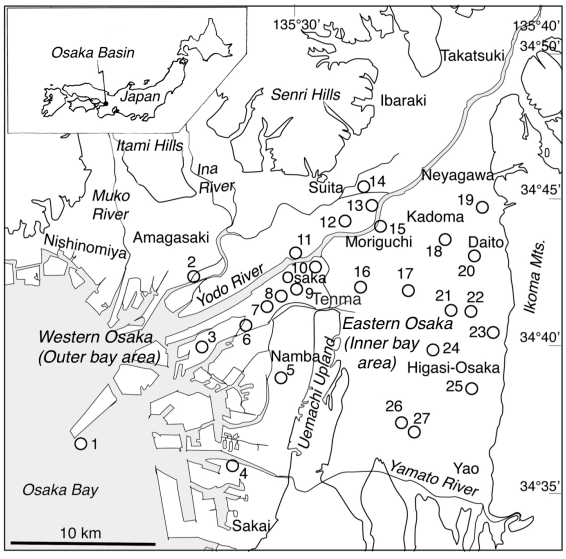

Figure 1. Locations of the studied borehole core sites (1 to 27) on the Osaka Plain.

cores with many calibrated ^{14}C dates obtained by academic research studies [10]-[18]. We also used supplemental data from other boreholes containing the Kikai-Akahoya tephra layer (erupted 7300 cal y BP [19]) [20]-[23] and made accessorily use of uncalibrated ^{14}C dates [21] [24]. These borehole sites are 1: Off Yumeshima [14], 2: Tatsumibashi [24], 3: Shimaya [22], 4: Suminoe [11], 5: Kitatsumori [12] [25] [26], 6: Yoshino [15], 7: Fukushima [22], 8: Umeda [21], 9: Daisanbilu [27], 10: Nagara-Hachiman [17], 11: Shin-Yodogawa [13], 12: Houshin [16], 13: Ousumi [16], 14: Kitaeguchi [22], 15: Moriguchi [18], 16: Gamou, [15] 17: Mattamoroguchi [20], 18: Kadoma [22], 19: Neyagawa [22], 20: Daito [22], 21: Kawachino [15], 22: Kitamiya [15], 23: Kitoragawa [20], 24: Uryudou [20], 25: Ikeshima-Fukumanji [20], 26: Kami [20], and 27: Kyuhouji [20]; as shown in **Figure 1**.

The modern Osaka Plain can be divided into two areas of western and eastern areas by paleo-environmental characteristics. The western Osaka, as describe the outer bay area in this paper, includes the modern western Osaka Plain and Osaka Bay area, and the eastern Osaka, the inner bay area, includes the modern eastern Osaka Plain and/or Paleo-Kawachi Bay. The Uemachi Upland distributed in the central part of the studied area (**Figure 1**) and paleo-spit, called the Tenma Spit, extended northward from the upland, is a boundary between the inner bay and the outer bay areas.

2.2. Determination of Depositional Age

We used a method described previously [4] [28] to construct a depositional curve for each borehole core from the elevations of dated strata (calendar years) (**Figure 2**). The depositional curves were plotted as smoothed curves on an age versus elevation diagram. By referring to these curves, we could determine the depositional age of each horizon, and from the slope of the curve we could determine the depositional rate during each period. The paleo-water depth of the deposits was determined as previously described [4] [25] by comparing the depositional curves with the relative sea-level curve after 11,000 cal y BP in the Osaka Bay area [12] [26]. The paleo-water depth of each horizon was obtained by calculating the elevation difference between the position of the horizon on the depositional curve and sea level at the time of deposition (see **Figure 2**). In this study, paleo-water depth is considered to represent accommodation [29].

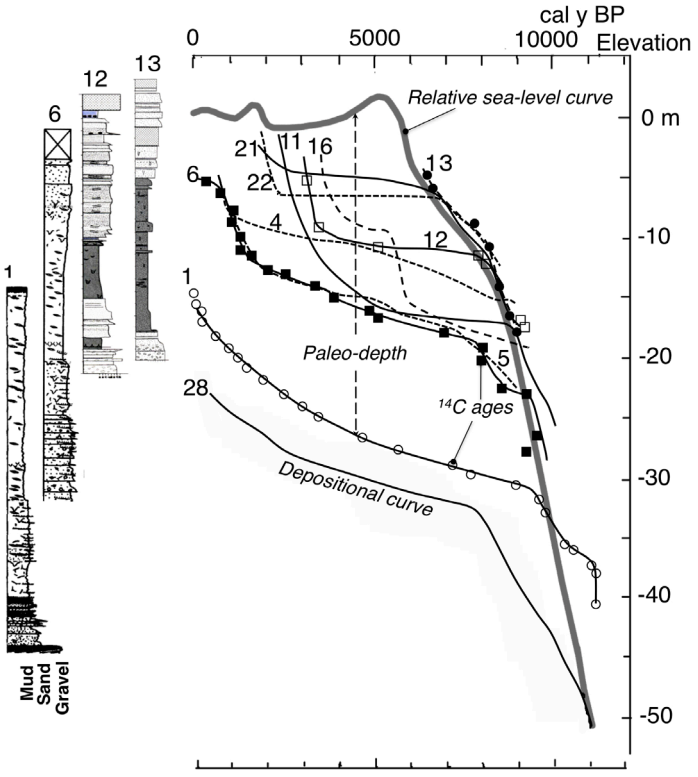

Figure 2. Relative sea-level curve for the Osaka Basin [12] and depositional curves on a elevation-age diagram and columnar sections at some borehole sites on the studied area. Curve of 28 is the Off-Kobe [10].

2.3. Construction of Paleo-Water Depth Maps

Paleo-water depth maps (**Figure 3**) were constructed for the following four time points, selected in part because abundant paleo-water depth data were available and the horizons were decided on easier: 1) 9000 cal y BP, when the marine transgression reached what is today the inland part of the modern Osaka Plain; 2) 7300 cal y BP, when the Kikai-Akahoya tephra was deposited (during the transgressive stage); 3) 5300 cal y BP, the age of the maximum flooding surface; and 4) 3500 cal y BP, the highstand and/or regressive stage, characterized by progradation of the river delta and costal line. At these four time points, sea level, obtained from the relative sea-level curve for Osaka Bay [12], was –20, –8, +3, and –1 m, respectively (**Figure 2**).

We used paleo-geomorphic data for the seafloor to construct the paleo-water depth (bathymetric) maps, in addition to the paleo-water depth data from the cores. For the map of 9000 cal y BP, we used the basement surface proposed sequence boundary between the latest Pleistocene and Holocene [24]. As the sequence boundary reflects erosion due to transgressive wave and tidal effects [23], we have to consider the topographies of pre-transgression, steeper slopes of drowned valley and coastal cliff. To draw the map for 7300 cal y BP, we referred to the map for 9000 cal y BP. We used the coastline at the maximum transgression [30] to draw the map for 5300 cal y BP. To construct the map of 3500 cal y BP, we drew the depth contours between those of the 5300 cal y BP bathymetry and the modern bay floor bathymetry of Osaka Bay. We also referred to the published geologic cross sections [23] [27] [31] [32] in constructing the paleo-water depth maps.

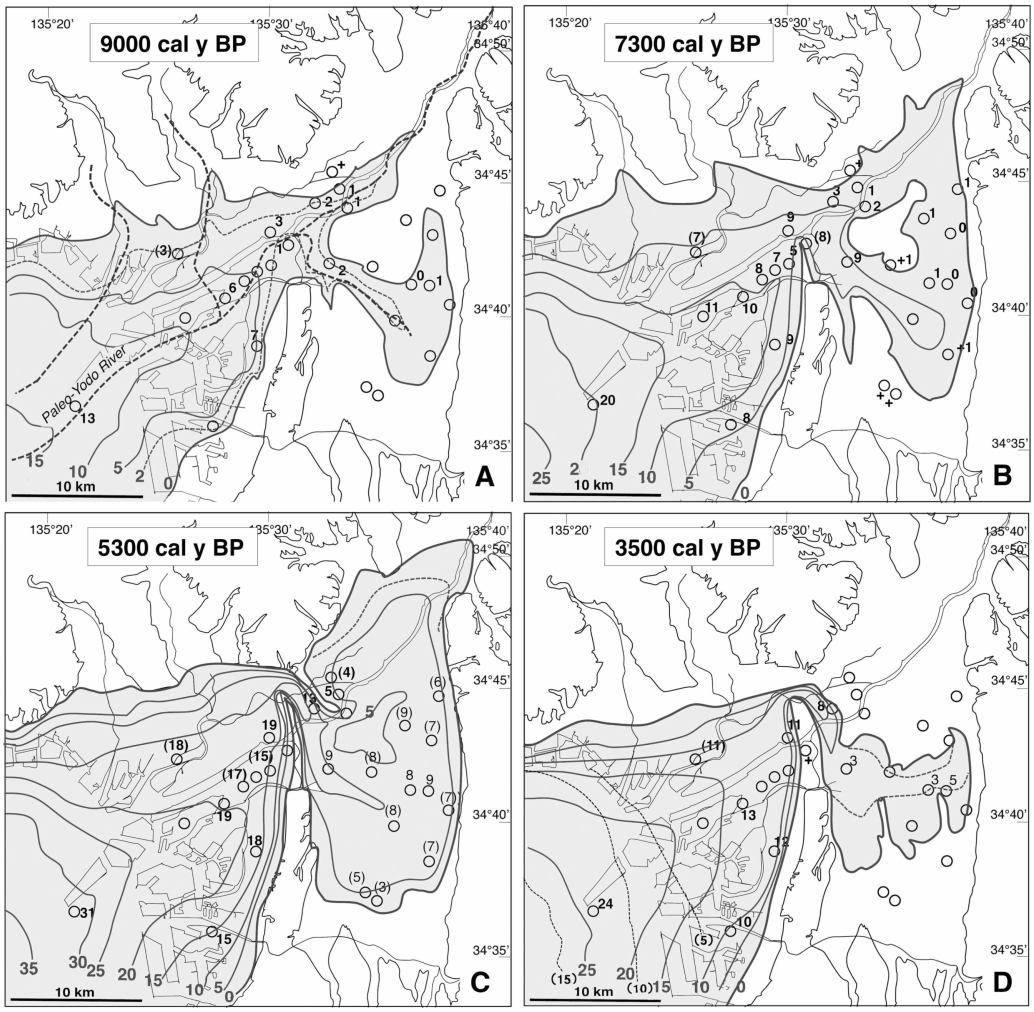

Figure 3. Maps of paleo-water depth (contours) at 9000, 7300, 5300, and 3500 cal y BP. Circles indicate borehole sites, and the adjacent numbers indicate the paleobathymetry (m) at the corresponding site. The paleo-Yodo River and other paleo-river channels are also shown in panel A.

2.4. Construction of Sediment Accumulation Maps

The sediment accumulation on the seafloor between each pair of time points (Figure 4) was determined by using the corresponding paleo-water depth maps, constructed as described before. The sediment accumulation between 3500 cal y BP and the present was obtained by using the paleo-water depth map for 3500 cal y BP and modern plain elevations and bay bathymetry of modern Osaka Bay. Temporal variations in the depositional rates and paleo-water depths at representative localities are shown in Figure 5. We also calculated the depositional rates (mm/y) per unit area between each pair of time points for the outer bay area (western Osaka), the inner bay area (eastern Osaka), and the whole study area (Figure 6).

3. Variations in Paleo-Water Depth and Sediment Accumulation

In the Osaka Basin, the post-glacial marine transgression began after 10,000 cal y BP and was followed by a period of maximum transgression from 6000 to 5000 cal y BP. The subsequent sea-level highstand and slight regression lasted until the present (Figure 2) [12]. In this section we describe temporal variations in paleo-water

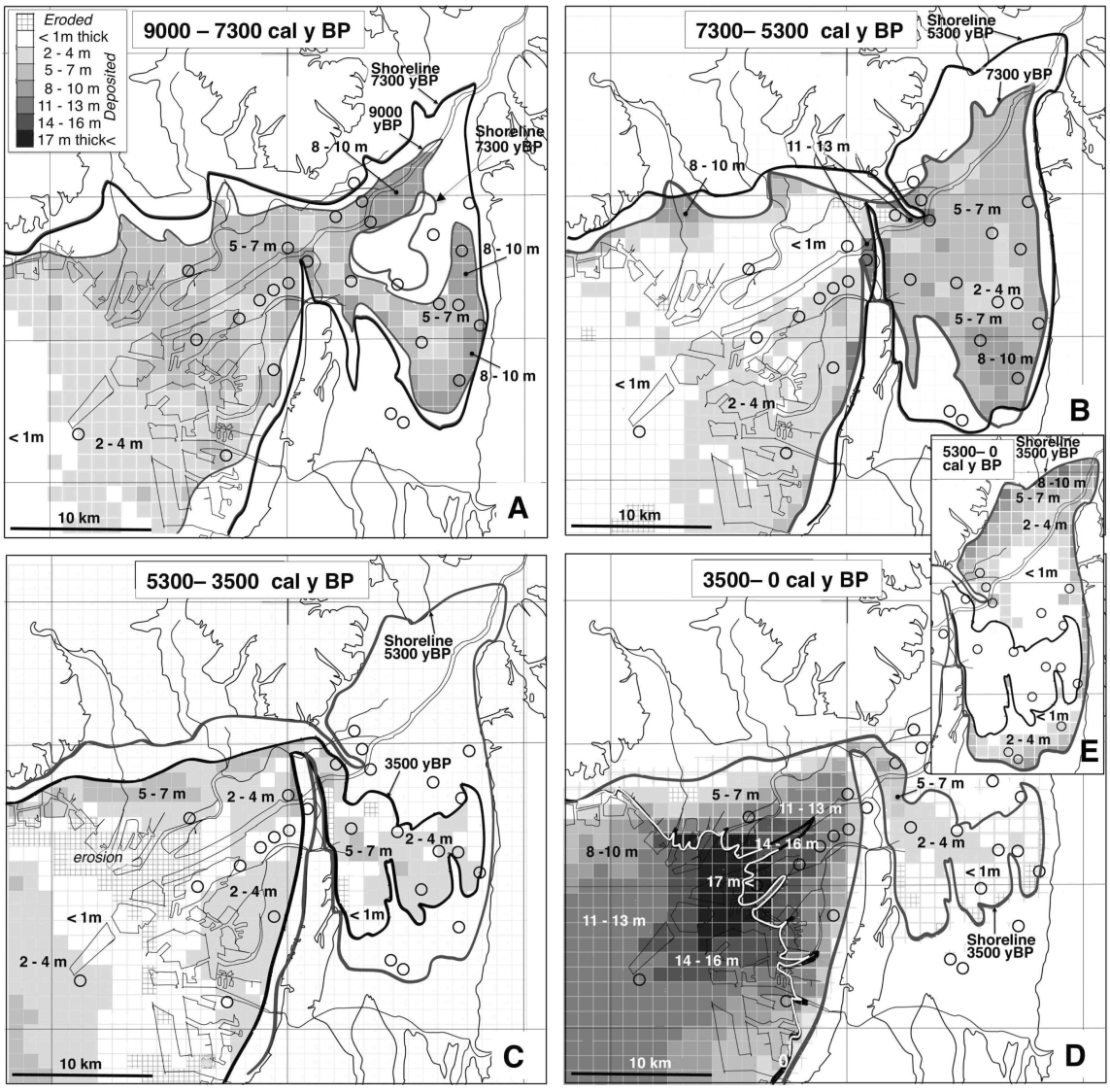

Figure 4. Maps showing the sediment accumulation during 9000 to 7300, 7300 to 5300, 5300 to 3500, 3500 cal y BP to the present, and 5300 cal y BP to the present. The gray scale shows the accumulated thickness (m) per 100 years during the ages.

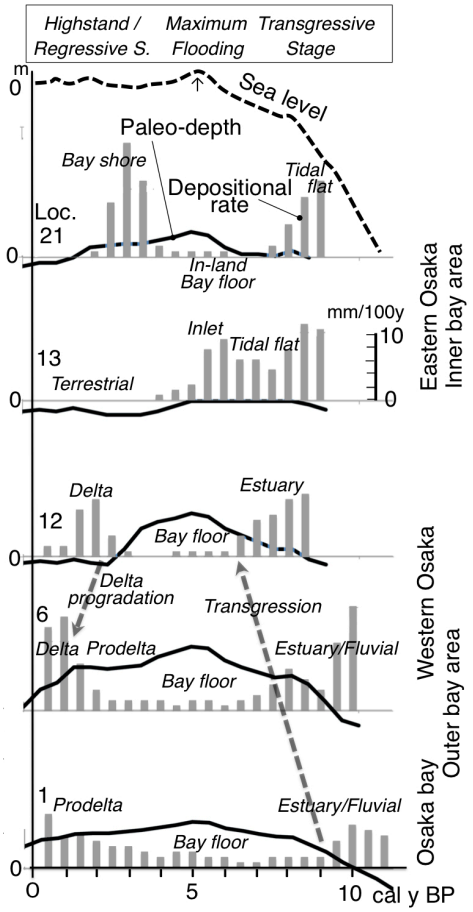

Figure 5. Temporal variations in paleo-water depth (m; bold black lines), depositional rate (mm/100y; gray bars) at some borehole sites and relative sea level curves (bold dashed line) in the Osaka Basin.

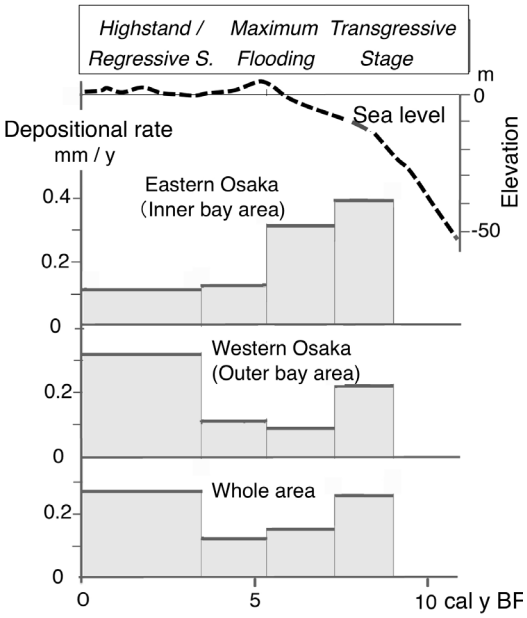

Figure 6. Temporal variations of depositional rates during these 9000 years in the eastern Osaka (inner bay area), western Osaka (outer bay area) and the whole Osaka basin.

depth and sediment accumulation during each of these stages (**Figures 3-6**).

3.1. Transgressive Period

From 9000 to 7300 cal y BP, sea level rose rapidly at a rate of 0.7 cm/y (**Figure 2**). The marine transgression in coastal areas is represented by a flat transgressive surface on the basement [23]. This surface, which was cut by wave and tidal erosion, is easily recognized in the stratigraphic sequence [27].

In the outer bay area of the western Osaka, the transgressive surface is found off Kobe at –51 m (relative to mean sea level) and its age is 11,000 cal y BP [10]; Off Yumeshima, it is at –37.2 m (10,800 cal y BP) [14]; in Shin-Yodogawa, it is at –22.5 m (9500 cal y BP) [13]; in Yoshino, at the mouth of the Yodo River, it is at –20.0 m (9200 cal y BP) [14]; and in Kitatsumori, Nishinari, it is at –22.0 m (9200 cal y BP) [12].

In the inner bay area of the eastern Osaka, transgression occurred later and the transgressive surface is at higher elevations compared with the outer bay area. About 9000 cal y BP, the ocean invaded the narrow, steep-walled incised valleys that had formed in the paleo-Osaka Plain during the glacial period (**Figure 3(A)**), and these valleys began to fill with sediment. From 9000 to 7300 cal y BP, sediment accumulation was highest in the shallow waters in the area of the paleo-Yodo River mouth and in the estuary of inner bay area (**Figure 4(A)**). In the small inner bay, muddy deposits 5 - 10 m thick accumulated in tidal flats, where the water was less than 2 m deep (**Figure 3(A)** and **Figure 4(A)**). As transgression progressed, the area of deep water expanded and sediment accumulation decreased (**Figure 5**).

At about 7300 cal y BP, water depths in the outer bay exceeded 5 m (**Figure 3(B)**), and in these calm, deeper waters, the amount and rate of deposition decreased (**Figure 4(B)** and **Figure 5**). In contrast, in the inner bay (eastern Osaka) area, the accumulated deposits are twice as thick (2 to 10 m; **Figure 4(B)**) as in the outer bay (**Figure 5**). Rapid deposition continued in muddy tidal flats in coastal areas of the inner bay.

From 7300 to 5300 cal y BP, the rate of sea-level rise increased to 1 cm/y (**Figure 2**). Around 5300 cal y BP, at water depths of 25 to 35 m in the outer bay area (**Figure 3(C)**), the sediment accumulation rate was slow, about 40% of that during the early transgression (**Figures 4(B)-(C)**, and **Figure 5**. In the small and shallow inner bay, the tidal flats were replaced by expanded Kawachi Bay with a water depth of 5 to 10 m (**Figure 3(C)**). During this period, thick (5 to 10 m) mud was deposited in the inner bay, and the deposition rate was about four times that in the outer bay (**Figure 4(B)**, **Figure 5** and **Figure 6**). Thus, most suspended sediments from the major rivers (the Yodo and Yamato rivers) were deposited in inner Kawachi Bay during this time interval [26].

3.2. Maximum Transgression

Maximum flooding occurred from 6000 to 5000 cal y BP in the modern Osaka Plain area [12]. Maps showing the coastline during this period have been published previously [21] [30]. At this time, in the shallow waters north of the Uemachi Upland a spit, called the Tenma Spit, formed between the inner bay and the outer bay. This spit, which was 7 to 8 km long and less than 100 m wide, extended northward from the northern end of the upland [27]. A shoal was in the Moriguchi and Kadoma area of the northwestern part of the inner bay area (**Figure 3(B)**) and the northern edge of the shoal had been eroded to a steep cliff by the Yodo River during the glacial period, as shown on a paleogeographic map [21].

At 5300 cal y BP, the age of the maximum flooding period, the water depth was 10 to 35 m in the outer paleo-Osaka Bay and 5 to 10 m in inner bay (**Figure 3(C)**), and both the depositional rate and sediment accumulation were low (**Figure 5** and **Figure 6**).

3.3. Highstand and Regression

After 5300 cal y BP, the area occupied by the inner bay (Kawachi Bay) gradually decreased. By 3500 cal y BP, sea level had decreased to 3 to 4 m below the highstand (**Figure 2**), and the inner bay had become the brackish Kawachi Lagoon [30]. This lagoon was only about 3 m deep (**Figure 3(D)**), and tidal flats were widely distributed along its shores [16]. In Kawachi Lagoon, 1 to 5 m of sand and mud was deposited between 5300 and 3500 cal y BP (**Figure 4(C)**). This amount of deposition was only one-third to one-fourth the amount deposited during the transgressive stage (**Figure 5** and **Figure 6**). In the whole Osaka area, the sediment accumulation decreased; in many areas less than 5 m of sediment was deposited (**Figure 6**).

From 3500 cal y BP to the present, the Yodo River delta has prograded into Osaka Bay [23]. Sandy delta

body deposits, 10 to 20 m thick, formed the modern Osaka Plain (**Figure 4(D)**). The sediment accumulation after 3500 cal y BP exceeded that during the transgressive stage by 30% - 40% (**Figure 6**), primarily because of the progradation of the river delta. In the inner bay area, the Kawachi Lagoon became the freshwater Kawachi Lake as regression progressed, and eventually the modern Kawachi Plain emerged. The sediment accumulation also decreased (**Figures 4(D)-(E)**). The prograding sediments and coastal system deposits during this period were composed primarily of sand and gravel. The Tenma Spit and the shallow shoreface of west of the Uemachi Upland became a strand plain under the regressive coastal regime [27].

3.4. Regional Differences of Accommodation and Sediment Accumulation

The variations in paleo-water depth and amounts of deposition in the Osaka basin differ regionally. In particular, the pattern of variation in accommodation and sediment accumulation differs between the outer bay area, western Osaka, and the inner bay area, eastern Osaka (**Figures 4-6**). The depositional rare in the outer bay area reached a maximum during the period of regression during the subsequent highstand and regression (**Figure 6**). By contrast, the depositional rate in the inner bay area was large in the early transgressive period, small during the period of maximum transgression, and reached a minimum during the subsequent highstand (**Figure 6**). The pattern of the variations in the basin overall was similar to that observed in the outer bay area (**Figure 6**). Moreover, the pattern of variation in depositional amounts during the latest Pleistocene to Holocene in the intra-arc Osaka basin is similar to the pattern predicted by depositional sequence models [1] [2].

4. Conclusions

This study presents temporal and spatial variations in paleo-water depth and sediment accumulation during the transgressive, highstand, and regressive stages of the latest Pleistocene to Holocene in the intra-arc Osaka basin. Paleo-water depths were smaller and sediment accumulations were greater in the early transgressive period, but later during the transgression, the outer bay expanded inland and became deeper. Sediment deposition decreased during transgression. The maximum paleo-water depth and minimum depositional rate were reached during the period of maximum transgression. During the subsequent sea-level highstand and regression, deposition increased rapidly as a result of river delta and coastal progradations.

Accommodation and sediment accumulations differed regionally between the outer bay area and the inner bay area. From the transgressive to the regressive stage, the sediment accumulation decreased in the inner bay area; in contrast, in the outer bay area and in the basin overall, deposition was high during the first part of the transgressive stage, decreased during the period of maximum transgression, and increased again during the following highstand and regression. Moreover, during the regressive stage, thick deposits were formed by fluvial delta progradation. As a result, sediment accumulation during this stage was 30% - 40% more than the accumulation during the transgressive stage.

References

[1] Van Wagoner, J.C., Posamentier, H.W., Mitchem, R.M., Vail, P.R., Sarg, J.F., Louit, T.S. and Hardengol, J. (1988) An Overview of the Fundamental of Sequence Stratigraphy and Key Definition: Sea Level Change- and Integrated Approach. *SEPM Special Publication*, **42**, 39-45.

[2] Vail, P.R., Audemard, F., Boeman, S.A., Eisner, P.N. and Perez-Cruz, C. (1991) The Stratigraphic Signatures of Tectonics, Eustasy and Sedimentology—An Overview. In: Einsele, G., Ricken, W. and Seilacher, A., Eds., *Cycles and Events in Stratigraphy*, **6**, Springer-Verlag, Berlin, 617-659.

[3] Masuda, F. and Ito, M. (1999) Contributions to Sequence Stratigraphy from the Quaternary Studies in Japan. *The Quaternary Research*, **38**, 184-193. http://dx.doi.org/10.4116/jaqua.38.184

[4] Masuda, F. (1998) Dynamic Stratigraphy Based on Highly Dense Data of ^{14}C Ages in the Holocene. *Journal of Geography*, **107**, 713-727. (In Japanese with English Abstract or Summary) http://dx.doi.org/10.5026/jgeography.107.5_713

[5] Masuda, F. (2007) Formation of Depositional Sequences and Landforms Controlled by Relative Sea-Level Change: The Result of the Holocene to Upper Pleistocene Study in Japan. *Transactions, Japanese Geomorphological Union*, **28**, 365-379. (In Japanese with English Abstract or Summary)

[6] Masuda, F. and Saito, Y. (1999) Temporal Variations in Depositional Rates within a Holocene Sequence in Japan. *Proceeding of International Symposium of Prof. K.O. Emery Commemorative Workshop on Land-Sea Link in Asia*, **85**,

421-426.

[7] Naruse, Y. (1982) The Quaternary. Iwanami-Shoten, Tokyo, 269 p. (In Japanese)

[8] Iseki, K. (1983) Alluvial Plain. UP Earth Science, Tokyo University Press, Tokyo, 145 p. (In Japanese)

[9] Umitsu, M. (1994) Late Quaternary Environment and Landform Evolution of Riverine Coastal Lowlands. Kokonsyoin, Tokyo, 270 p. (In Japanese)

[10] Masuda, F., Miyahara, B., Hirotsu, J., Irizuki, T., Iwabuchi, Y. and Yoshikawa, S. (2000) Temporal Variation of Holocene Osaka Bay Conditions Estimated from a Core in Off-Kobe. *Journal of Geological Society of Japan*, **106**, 482-488. (In Japanese with English Abstract or Summary) http://dx.doi.org/10.5575/geosoc.106.482

[11] Nanayama, F., Doi, Y., Kitada, N. and Takemura, K. (2001) Stratigraphic, Sequence Stratigraphic and Sedimentary Environment Analyses on the Late Pleistocene Holocene Sediments of the Eastern Side of Osaka Bay, Central Japan since 130 Ka. *Journal of Geological Society of Japan*, **107**, 179-197. (In Japanese) http://dx.doi.org/10.5575/geosoc.107.179

[12] Masuda, F., Irizuki, T., Fujiwara, O., Miyahara, B. and Yoshikawa, S. (2002) A Holocene Sea-Level Curve Constructed from a Single Core at Osaka, Japan (A Preliminary Note). *Memoirs of Faculty of Science, Kyoto University, Series of Geology & Mineralogy*, **59**, 1-8.

[13] Sugiyama, Y., Nanayama, F., Miura, K., Yoshikawa, T., Yokota, H., Suehiro, M., Furutani, M., Tochimoto, Y., Hirose, K., Yokoyama, Y., Kitada, N. and Takemura, K. (2003) Complementary Study of the Uemachi Fault System in the Osaka BASIN (2): Evaluation of the Fault Activity Based on Supplementary Boring and Re-Interpretation of S-Wave Seismic Reflection Data. *Annual Report on Active Fault and Paleoearthquake Researches*, No. 11, 117-143. (In Japanese)

[14] Yoshikawa, S., Mitamura, M., Tanaka, Y. and Tsukada, Y. (2005) Sedimentary Facies and Radiocarbon Dates of the Yumeshima-Oki Core from Osaka Bay, Central Japan. *Proceeding of the* 15*th Symposium on Geo-Environments and Geo-Technics*, Yokohama, 10-11 December 2005, 173-178. (In Japanese)

[15] Mitamura, M., Tsukada, Y., Oshima, A., Sanbe, Y., Kitada, N. and Yoshikawa, S. (2009) Depositional Environment and Physical Property of the Chuseki-So in the Osaka Plain. *Proceedings of Symposium on Ground and Environmental Features*, Osaka, March 2009, 27-32. (In Japanese)

[16] Masuda, F. (2013) Depositional Environments of the Holocene Marine Clay Bed, Ma13 Bed Intercalated in the So-Called "Chuseki-So" of the Osaka Plain Analyzed by the Depositional Curves. *The Science and Engineering Review of Doshisha University*, **54**, 59-65.

[17] Research and Development Bureau of Ministry of Education, Culture, Sports, Science and Technology and Disaster Prevention Research Institute Kyoto University (2013) Report of Survey and Observation for Uemachi Fault Belt, 449 p. (In Japanese)

[18] Tsujimoto, A., Kitamura, S. and Yoshikawa, S. (2009) Variation of Depositional Environments of the Subsurface Chuseki-So in the Osaka Plain Analyzed by Micro Fossils. *Proceedings of Symposium on Ground and Environmental Features*, Osaka, March 2009, 27-32. (In Japanese)

[19] Machida, H. and Arai, F. (1992) Atlas of Tephra in and around Japan. Tokyo University Press, Tokyo, 336 p. (In Japanese)

[20] Chou, T. (2001) Origin of the Morishoji Site. In: *Archaeological Reports of the Morishoji Site in Osaka, Japan*, Osaka City Cultural Properties Association, Osaka, 49-51. (In Japanese)

[21] Mitamura, M., Matsuyama, N., Nakagawa, K., Yamamoto, K. and Suwa, S. (1994) Stratigraphy and Subsurface Structure of Holocene Deposits around Uemachi Upland in the Central Osaka Plain. *Journal of Geosciences, Osaka City University*, **37**, 183-212.

[22] Kansai Geo-Informatics Research Committee (2007) Kansai Jiban-Osaka Plain and Osaka Bay. Kansai Geoinformatics Council, Kansai, 345 p. (In Japanese)

[23] Masuda, F., Sato, T., Ito, Y. and Sakurai, M. (2013) Preliminary Note on a New Shazam Stratigraphy Applied to a Borehole Database Analysis of Subsurface Geology in the Osaka Plain. *Journal of Geography*, **122**, 892-904. (In Japanese with English Abstract or Summary)

[24] Mitamura, M. and Hashimoto, M. (2004) Spatial Distribution with the Drilling Database on the Basal Gravel Bed of the Namba Formation in the Osaka Plain, Southwest Japan. *The Quaternary Research*, **45**, 253-264. (In Japanese with English Abstract or Summary) http://dx.doi.org/10.4116/jaqua.43.253

[25] Masuda, F. (2002) Variation of Oceanic Condition for Osaka Bay Estimated from Borehole Cores. *Proceeding of Symposium by Kansai Branch of Japan Society of Engineering Geology*, Osaka, July 2002, 117-127. (In Japanese)

[26] Masuda, F. and Miyahara, B. (2000) Depositional Facies and Processes of the Holocene Marine Clay in the Osaka Bay Area, Japan. *The Quaternary Research*, **39**, 349-355. (In Japanese with English Abstract or Summary)

http://dx.doi.org/10.4116/jaqua.39.349

[27] Masuda, F., Nakagawa, Y., Sakamoto, T., Ito, Y., Sakurai, M. and Mitamura, M. (2013) Tenma Spit Deposit in the Holocene of the Osaka Plain: Distribution and Stratigraphy. *Journal of the Sedimentological Society of Japan*, **72**, 115-123. (In Japanese with English Abstract or Summary) http://dx.doi.org/10.4096/jssj.72.115

[28] Fujiwara, O., Kamataki, T. and Masuda, F. (2004) Sedimentological Time-Averaging and ^{14}C Dating of Marine Shells. *Nuclear Instruments and Methods in Physics Research Section B*: *Beam Interactions with Materials and Atoms*, **223-224**, 540-544.

[29] Jervey, M.T. (1988) Quantitative Geological Modeling of Siliciclastic Rock Sequences and Their Seismic Expression. *SEPM Special Publication*, **42**, 47-69.

[30] Kajiyama, H. and Itihara, M. (1972) The Developmental History of the Osaka Plain with References to the Radio-Carbon Dates. *Memoirs of Geological Society of Japan*, **7**, 101-112. (In Japanese)

[31] Sakurai, M. and Masuda, F. (2013) Construction of Subsurface Geological Structures Using a Drilling Database: A Case Study for an Intra-Arc Basin, the Osaka Plain, Southwest Japan. *Open Journal of Geology*, **3**, 39-43. http://dx.doi.org/10.4236/ojg.2013.32006

[32] Sakurai, M. and Masuda, F. (2014) Reconstruction of Relative Tectonic Movements Using Transgressive Ravinement Erosion Surfaces: A Case Study for the Shallow Subsurface Geology of the Osaka Plain, Japan. *Journal of Earth Sciences and Geotechnical Engineering*, **4**, 17-24.

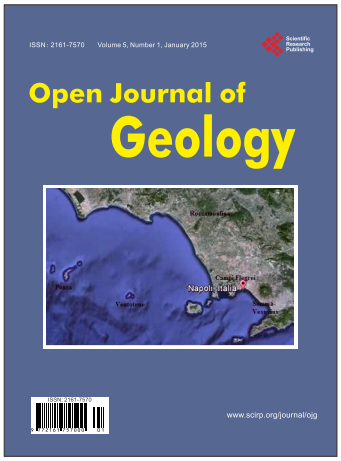

Call for Papers

Open Journal of Geology (OJG)

ISSN: 2161-7570 (Print) ISSN: 2161-7589 (Online)
http://www.scirp.org/journal/ojg

Open Journal of Geology **(OJG)** is an international journal dedicated to the latest advancement of geology. The goal of this journal is to provide a platform for scientists and academicians all over the world to promote, share, and discuss various new issues and developments in different areas of geology.

Subject Coverage

All manuscripts must be prepared in English, and are subject to a rigorous and fair peer-review process. Accepted papers will immediately appear online followed by printed hard copy. The journal publishes original papers including but not limited to the following fields:

- Earth science
- Economic geology
- Engineering geology
- Environmental geology
- Geoarchaeology
- Geochemistry
- Geochronology
- Geodetics
- Geography
- Geological modelling
- Geometallurgy
- Geomicrobiology
- Geomorphology
- Geomythology
- Geophysics
- Glaciology
- Historical geology
- Hydrogeology
- Meteorology
- Mineralogy
- Mining geology
- Oceanography
- Paleoclimatology
- Paleontology
- Petroleum geology
- Petrology
- Petrophysics
- Plate tectonics
- Sedimentology
- Seismology
- Soil science
- Speleology
- Stratigraphy
- Structural geology
- Volcanology

We are also interested in: 1) Short Reports—2-5 page papers where an author can either present an idea with theoretical background but has not yet completed the research needed for a complete paper or preliminary data; 2) Book Reviews—Comments and critiques.

Notes for Intending Authors

Submitted papers should not have been previously published nor be currently under consideration for publication elsewhere. Paper submission will be handled electronically through the website. All papers are refereed through a peer review process. For more details about the submissions, please access the website.

Website and E-Mail

http://www.scirp.org/journal/ojg **E-mail: ojg@scirp.org**

What is SCIRP?

Scientific Research Publishing (SCIRP) is one of the largest Open Access journal publishers. It is currently publishing more than 200 open access, online, peer-reviewed journals covering a wide range of academic disciplines. SCIRP serves the worldwide academic communities and contributes to the progress and application of science with its publication.

What is Open Access?

All original research papers published by SCIRP are made freely and permanently accessible online immediately upon publication. To be able to provide open access journals, SCIRP defrays operation costs from authors and subscription charges only for its printed version. Open access publishing allows an immediate, worldwide, barrier-free, open access to the full text of research papers, which is in the best interests of the scientific community.

- High visibility for maximum global exposure with open access publishing model
- Rigorous peer review of research papers
- Prompt faster publication with less cost
- Guaranteed targeted, multidisciplinary audience

Scientific Research

Website: http://www.scirp.org

Subscription: sub@scirp.org

Advertisement: service@scirp.org